iScience

CellPress

Article

Hydrogel Microfilaments toward Intradermal Health Monitoring

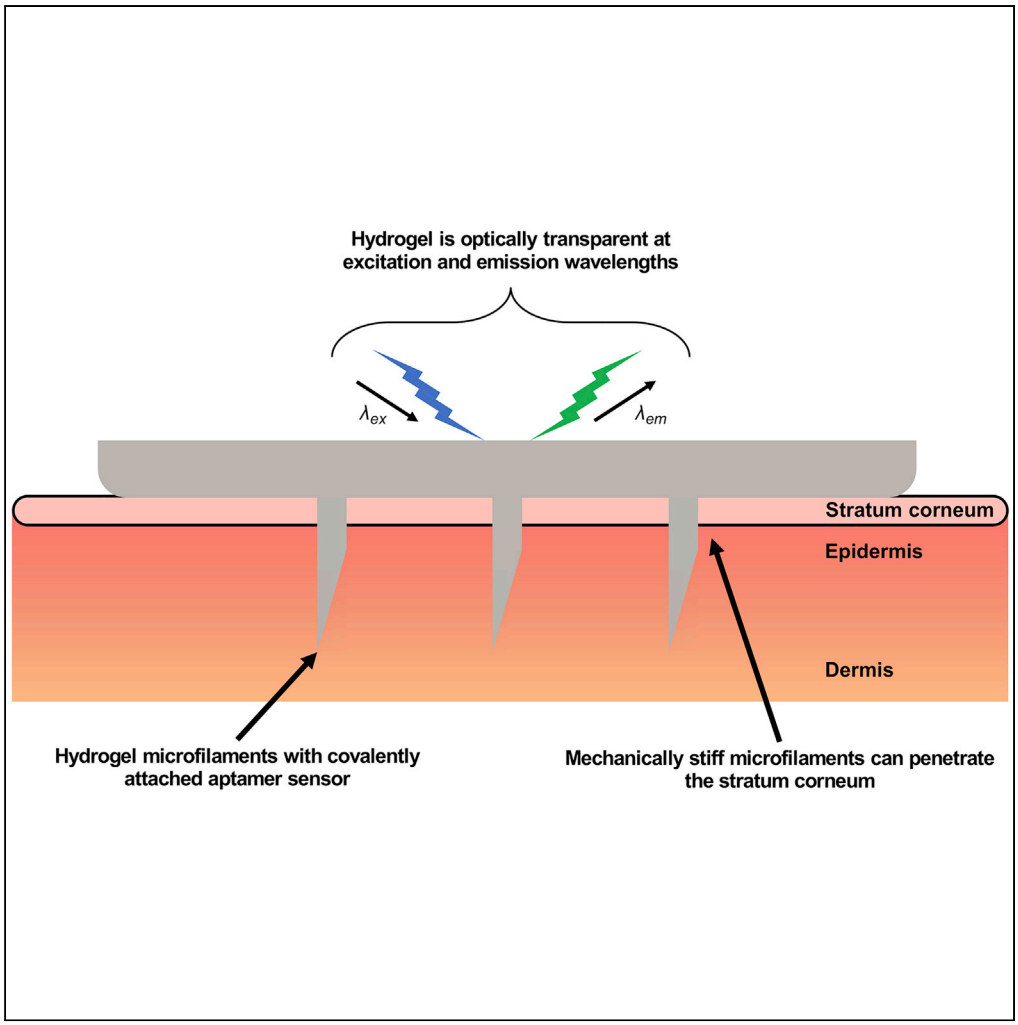

Nalin Tejavibulya, David A.M. Colburn, Francis A. Marcogliese, ..., Shilpika Chowdhury, Milan N. Stojanovic, Samuel K. Sia

ss2735@columbia.edu

HIGHLIGHTS

Polyacrylamide hydrogel microfilaments were fabricated via replica molding

Microfilaments are stiff, when dehydrated, and optically transparent, when hydrated

Fluorescent aptamer can be tethered to hydrogel matrix for *in situ* analyte sensing

Microfilaments penetrate skin with low pain and contact interstitial fluid

Tejavibulya et al., iScience *21*, 328–340
November 22, 2019
https://doi.org/10.1016/j.isci.2019.10.036

iScience

CellPress

Article

Hydrogel Microfilaments toward Intradermal Health Monitoring

Nalin Tejavibulya,[1,3] David A.M. Colburn,[1,3] Francis A. Marcogliese,[1] Kyung-Ae Yang,[2] Vincent Guo,[1] Shilpika Chowdhury,[1] Milan N. Stojanovic,[1,2] and Samuel K. Sia[1,4,*]

SUMMARY

Digital health promises a paradigm shift for medicine where biomarkers in individuals are continuously monitored to improve diagnosis and treatment of disease. To that end, a technology for minimally invasive quantification of endogenous analytes in bodily fluids will be required. Here, we describe a strategy for designing and fabricating hydrogel microfilaments that can penetrate the skin while allowing for optical fluorescence sensing. The polyacrylamide formulation was selected to provide high elastic modulus in the dehydrated state and optical transparency in the hydrated state. The microfilaments can be covalently tethered to a fluorescent aptamer to enable functional sensing. The microfilament array can penetrate the skin with low pain and without breaking, contact the dermal interstitial fluid, and be easily removed from the skin. In the future, hydrogel microfilaments could be integrated with a wearable fluorometer to serve as a platform for continuous, minimally invasive monitoring of intradermal biomarkers.

INTRODUCTION

The emerging paradigm of digital health will require minimally invasive techniques for continuous sensing of biomarkers in internal bodily fluids such as interstitial fluid and blood. A commonly used technology is continuous glucose monitors (CGMs), which monitor glucose levels in the interstitial fluid with high accuracy (Slattery and Choudhary, 2017; Forlenza et al., 2017; Welsh et al., 2019a, 2019b). However, insertion is painful and the device can cause discomfort during use (Slattery and Choudhary, 2017; Forlenza et al., 2017; Ramchandani et al., 2011), such that up to 41% of diabetic patients have discontinued the use of CGMs (Slattery and Choudhary, 2017). In alternative approaches, noninvasive monitoring of analytes in extracorporeal fluids such as sweat (Alizadeh et al., 2018; Currano et al., 2018; Nyein et al., 2018; Parlak et al., 2018) must account for physiological variables such as differing sweat secretion rates and compositions among individuals and daily conditions (Nyein et al., 2018; Alizadeh et al., 2018).

This tradeoff in comfort against accuracy has motivated the development of microneedles that can painlessly interface with the interstitial fluid to facilitate accurate and continuous monitoring. Although most applications of microneedles have focused on delivery of drugs or vaccines (Yan et al., 2010; Chen et al., 2009; Sullivan et al., 2010; Yu et al., 2015; Ito et al., 2012, Mcvey et al., 2014), other works have focused on sampling of blood (Li et al., 2009, 2013; Tsuchiya et al., 2007) and interstitial fluid (Mukerjee et al., 2004; Yang et al., 2013; Caffarel-Salvador et al., 2015) for analyte sensing. Such approaches include hollow microneedle arrays for fluid collection with off-site analysis (Blicharz et al., 2018; Li et al., 2013), solid arrays for skin pre-treatment before fluid collection (Wang et al., 2005), and integrated sampling and sensing approaches (Windmiller et al., 2011; Zahn et al., 2005; Invernale et al., 2014; Jina et al., 2014). Although the fluid extraction process in traditional microneedles is minimally invasive, current challenges include reliability, contamination, and variable yield (often less than 10 μL for interstitial fluid) (Kiang et al., 2017; Lei and Prow, 2019). Further, integrated sampling and sensing approaches are susceptible to delayed sensing as the fluid is transported to an external electrochemical sensor. Thus, an *in situ* approach—where the sensing takes place within the interstitial fluid, without the need to transport the fluid elsewhere—could be more suitable for continuous sensing.

Hydrogels have great potential for *in situ* biosensing because of their biocompatibility, hydrophilicity, and tunable structure (Le Goff et al., 2015). Moreover, fluorescent nanoparticles or sensors can be incorporated into the hydrogel matrix to enable *in situ* sensing of multiple analytes (Park and Park, 2018; Tan et al., 2016). To date, many applications of hydrogels require injection (Kanick et al., 2019; Chien et al., 2017), which is invasive and makes the hydrogel difficult to remove. In addition, fluorescent sensors can diffuse out of the

[1]Department of Biomedical Engineering, Columbia University, 351 Engineering Terrace, 1210 Amsterdam Avenue, New York, NY 10027, USA

[2]Division of Experimental Therapeutics, Department of Medicine, Columbia University, New York, NY 10032, USA

[3]These authors contributed equally

[4]Lead Contact

*Correspondence: ss2735@columbia.edu

https://doi.org/10.1016/j.isci.2019.10.036

hydrogel, resulting in a loss of signal and limiting the operation lifetime (Li et al., 2019). Here, we describe a strategy for fabricating hydrogel structures toward *in situ* sensing in the body without invasive injection or removal of the hydrogel. The proposed structures are sufficiently stiff and sharp to penetrate the skin to directly access interstitial fluid and can be covalently conjugated to fluorescent sensors for sustained sensing.

RESULTS AND DISCUSSION

Design and Fabrication of Array of Stiff and Sharp Hydrogel Microfilaments

Our design consists of an array of hydrogel "microfilaments" that are chemically tethered to fluorescent sensors, which rapidly respond to analyte levels. In contrast to traditional hollow silicon-based microneedles, the hydrogel microfilaments are non-hollow and porous. Whereas silicon-based microneedles require a complex scheme for fabrication and extraction of fluid for sensing, the non-hollow structure of the microfilaments allows for easy fabrication (via molding, for example) and the porosity ensures that analytes can diffuse into the filaments and interact with conjugated sensor molecules. Further, the microfilaments are designed to be mechanically stiff in the dehydrated state and soft in the hydrated state (i.e. upon contact with internal bodily fluids). We chose polyacrylamide as the hydrogel material, as acrylamide-based copolymers are biocompatible and used in Food and Drug Administration (FDA)-approved medical devices for prolonged wear (such as soft contact lenses (Nicolson and Vogt, 2001) and urinary incontinence treatment devices (Toozs-Hobson et al., 2012)). However, the hydrogel, which is soft in the hydrated state, must overcome the skin's compliant surface before penetrating the stratum corneum (Park and Prausnitz, 2010) and contacting dermal interstitial fluid.

As such, we fabricated stiff and sharp hydrogel structures by using desiccated high-percentage polyacrylamide, which provides high mechanical strength and stiffness, and fashioning beveled tips in order to minimize the insertion force. Geometrically, the hydrated microfilaments are 1,500 μm tall and 300 μm in diameter (i.e. exhibiting an aspect ratio of 5) and have a 74° diamond-shaped bevel. (The dimensions of the desiccated, de-swelled microfilaments were approximately 1,100 μm in height and 200 μm in diameter.) The designed depth ensured contact with dermal interstitial fluid, the total volume ensured a sufficiently large fluorescence signal from the conjugated fluorescent sensor, and the bevel ensured piercing of the stratum corneum. We placed the polyacrylamide microfilaments into an array with a diameter of 7 mm, containing 9 microfilaments that are spaced 1,500 μm apart tip-to-tip and placed in a 3 × 3 configuration. The hydrogel microfilament array was fabricated via molding (Figure 1A). Positive microfilament array molds were designed using SolidWorks CAD software (Figure 1B) and produced by CNC milling of machinable acrylic plastic (Figure 1C). Compared with fabrication techniques used to fabricate silicon-based microneedles (Barrett et al., 2015), CNC milling of acrylic molds (Guckenberger et al., 2015) is simple to perform, cost-effective, and allows for high-aspect geometry. Acrylic plastic was chosen as the mold due to its ease of machinability for fine features, particularly a diamond-shaped bevel at the end of the hydrogel microfilament for ease of insertion into the skin. We chose a 5-bevel design, as they have been shown to be less painful when compared with traditional 3-bevel designs (Hirsch et al., 2012). A silicone negative mold (Figure 1D) is then replicated from the positive mold.

The sensor-laden polyacrylamide microfilament array was formed by casting a mixture of methacryl-functionalized fluorescent sensor and polyacrylamide precursor solution in the negative silicone mold followed by exposure to collimated ultraviolet (UV) light. The polyacrylamide precursor solution was composed of 30% w/v acrylamide, 2% w/v cross-linking agent (N,N'-methylenebisacrylamide), 0.5% v/v photoinitiator (2-hydroxy-2-methylpropiophenone, or Darocur 1173), and 100 nM fluorescent sensor. The microfilament array was extracted immediately after photopolymerization and subsequently rinsed under vacuum in two fresh baths of phosphate-buffered saline (PBS) to remove unpolymerized polyacrylamide precursor residues. The hydrogel was then desiccated to dry and harden the microfilaments, yielding the final sensor-conjugated microfilament array (Figure 1E).

Optimization of Polymer Formulation for Optical, Swelling, and Mechanical Properties

In addition to biocompatibility (Hadjesfandiari and Parambath, 2018) and mechanical strength, polyacrylamide, as used in the microfilaments, offers favorable diffusive and optical properties for real-time sensing *in situ*. It has high porosity (Holmes and Stellwagen, 1991) to enable diffusion of analytes from the dermal interstitial fluid to the aptamer sensor and is optically transparent to enable transmission of light. The optical and mechanical properties can be easily tuned by controlling the monomer formulation, specifically

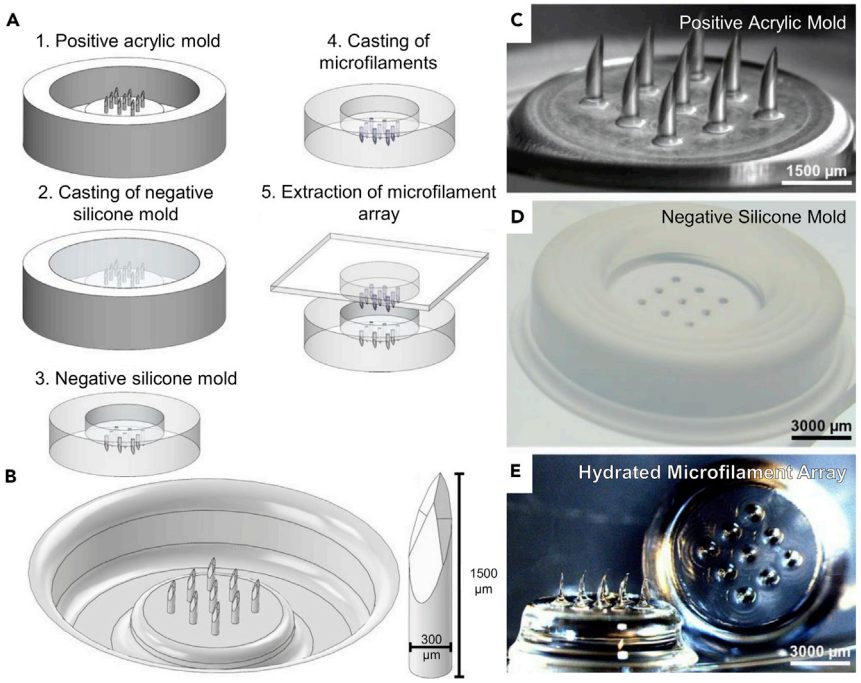

Figure 1. Fabrication of Hydrogel Microfilament Arrays

(A) Schematic diagram of the fabrication process for hydrogel microfilament arrays.

(B) CAD design for a microfilament array in the hydrated state.

(C) Positive acrylic mold fabricated via CNC milling.

(D) Negative silicone mold, using a fast-curing platinum-cured silicone.

(E) Fabricated microfilament array in the hydrated state.

the acrylamide percentage (%AAm) as well as the ratio of acrylamide to N,N′-methylenebisacrylamide cross-linker (AAm/MBAm) (Bansil and Gupta, 1980). Figure 2A summarizes the optical and mechanical properties that were considered for optimization of the polymer formulation. To determine the hydrogel composition that would yield desirable optical properties, the absorbance of different hydrogel compositions was measured using the microplate reader. Measurement of absorbance at the peak excitation and emission wavelengths for 6-carboxyfluorescein (FAM) and 6-carboxytetramethylrhodamine (TAMRA) fluorophores was performed on a range of polyacrylamide compositions that polymerize without leaving opaque residue (Figure 2B). Excessively high acrylamide concentration or insufficient cross-linker leaves acrylamide unpolymerized, leading to opaque and brittle hydrogel; the limit was found to be around 32% w/v acrylamide. These absorbance measurements were then used to calculate the percent transmittance at the specified wavelengths (Figure S1). Both %AAm and AAm/MBAm significantly affected absorbance ($p < 0.0001$). For a set %AAm, absorbance decreased with increasing AAm/MBAm values; for example, absorbance decreased ($p < 0.05$) for all wavelengths assessed when AAm/MBAm values increased from 10 to 20 (at a fixed %AAm). To simplify measurements of the other parameters in the subsequent experiments, only formulations with AAm/MBAm ratios of 15, 17.5, and 20 and %AAm of 20, 25, and 30 were selected. The absorbance values at 470 nm, 520 nm, 550 nm, and 580 nm for these polyacrylamide compositions are summarized in Table S1.

Microfilament integrity during insertion is facilitated by having sharp tips to minimize the insertion force and overcome the skin's compliant surface (Park and Prausnitz, 2010). Hydrogels typically have high water content. As such, when left to desiccate, significant deformation in shape of the hydrogels is observed. Since morphology retention is necessary to preserve the beveled tip for easy insertion, it is important to understand the extent of shrinking and the effect on microfilament morphology following desiccation. Figure 2C shows the shrinkage percentage of different polyacrylamide compositions, as determined by the change in radius before and after hydrogel desiccation. Polyacrylamide formed from precursor solutions containing higher %AAm exhibit significantly ($p < 0.0001$) decreased shrinkage percentage for all AAm/MBAm ratios tested, likely due to an increase in dry weight that inhibits collapse of the matrix upon

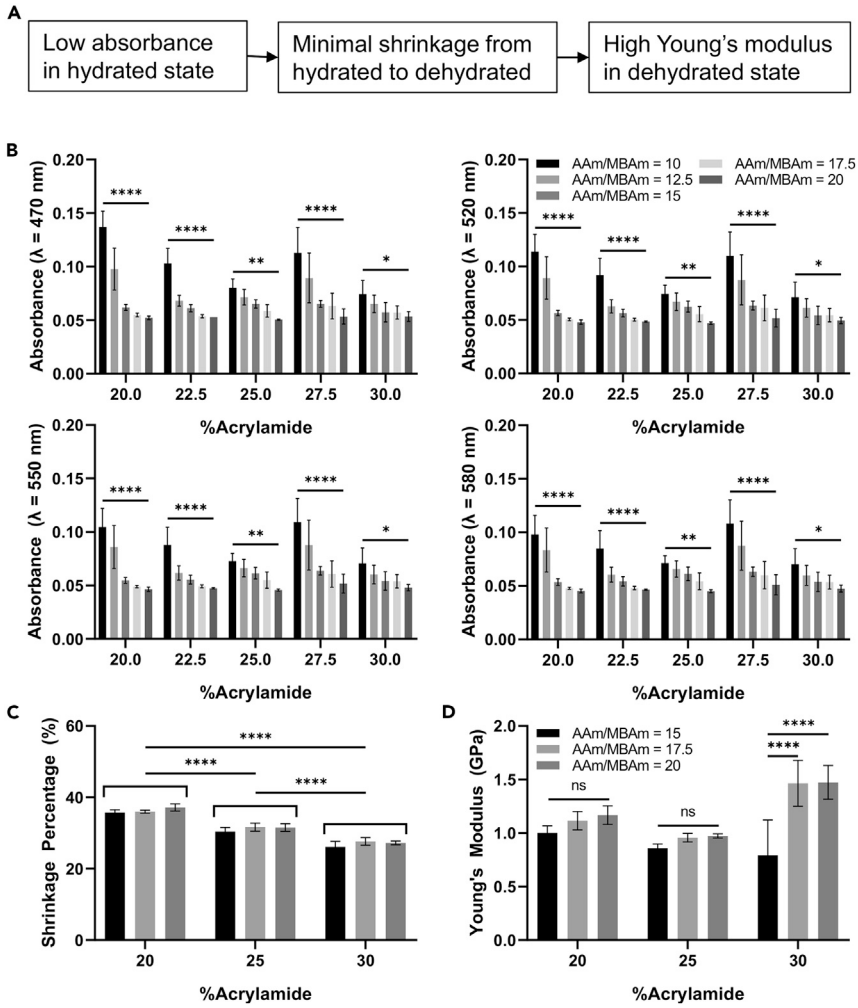

Figure 2. Optical and Mechanical Properties of Polyacrylamide Hydrogel

(A) Design criteria selected for optimization of polyacrylamide formulation.

(B) Absorbance values of hydrated polyacrylamide disks with different formulations. Top left: λ = 470 nm, the excitation wavelength for FAM (n = 4). Top right: λ = 520 nm, the emission wavelength for FAM (n = 4). Bottom left: λ = 550 nm, the excitation wavelength for TAMRA (n = 4). Bottom right: λ = 580 nm, the emission wavelength for TAMRA (n = 4). See also Figure S1 and Table S1.

(C) The shrinkage percentage of polyacrylamide hydrogel for different polymer formulations (n = 6). See also Figure S2

(D) The Young's modulus of dehydrated polyacrylamide hydrogel for different polymer formulations (n = 4). Data analyzed using a two-way ANOVA with Tukey post-hoc test. "ns" indicates not significant, "*" indicates significant at $p < 0.05$, "**" indicates significant at $p < 0.01$, and "****" indicates significant at $p < 0.0001$. Line indicates comparison between groups. Data are represented as mean ± standard deviation.

dehydration. A scanning electron microscopic (SEM) image of a polyacrylamide microfilament array taken two days after fabrication (Figure S2) demonstrated that challenging features for microfabrication—such as high aspect ratio, diamond-shaped bevels, and sharp tips—are preserved after shrinkage as brought on by desiccation.

In addition to having a sharp, beveled tip, the microfilaments must have high mechanical strength to penetrate the skin and access dermal interstitial fluid. In its hydrated state, polyacrylamide is soft and unable to pierce the skin. Although there has been recent effort to develop hydrated hydrogels with good mechanical properties, such as high compressive strength or Young's modulus, by modifying polymer formulation or polymerization method (Zhao, 2017), we optimized the polyacrylamide formulation to yield desired mechanical properties in the dehydrated state. Because the material hardens when low in water content,

		Composition	
		%AAm = 30 and AAm/MBAm = 15	
Optical	Absorbance, transmittance at 470 nm	0.058 ± 0.009	87.614 ± 1.820%
	Absorbance, transmittance at 520 nm	0.054 ± 0.009	88.270 ± 1.735%
	Absorbance, transmittance at 550 nm	0.054 ± 0.009	86.801 ± 1.090%
	Absorbance, transmittance at 580 nm	0.054 ± 0.009	88.373 ± 1.798%
Mechanical	Young's modulus	0.793 ± 0.329 GPa	
Deformation	Shrinkage percentage	26.115 ± 1.547%	

Table 1. Properties of Polyacrylamide of Composition %AAm = 30 and AAm/MBAm = 15

Summary of properties for selected polyacrylamide formulation with 30% acrylamide (%AAm) and acrylamide to N,N'-methylenebisacrylamide cross-linker ratio (AAm/MBAm) of 15. Data are represented as mean ± standard deviation.

desiccated polyacrylamide microfilaments are able to penetrate the stratum corneum. To quantify the strength of the desiccated microfilaments, the Young's modulus was determined experimentally at different polyacrylamide compositions. Figure 2D shows that all the compositions selected based on highest optical transmission exhibit comparable and extremely high Young's modulus of approximately 1 GPa. These values are approximately one order of magnitude less than hard plastic (Crompton, 2012) and indicate that desiccated polyacrylamide is much stiffer than PDMS (Johnston et al., 2014). Conversely, in the hydrated state, the hydrogel has a Young's modulus of 461 ± 76 KPa, matching more closely that of surrounding skin (~100 kPa (Liang and Boppart, 2010)) and hence reducing the risk of immune response due to mechanical mismatch (Stieglitz and Schuettler, 2013). At fixed %AAm, Young's modulus increased with AAm/MBAm ratio, presumably due to decrease in cross-linked clusters that introduce heterogeneity and soften the matrix (Denisin and Pruitt, 2016). Overall, any of the tested formulations may be used to fabricate the microfilament sensing platform with sufficiently high mechanical strength to penetrate the stratum corneum of the human skin.

Ultimately, the choice of polymer composition for microfilament fabrication is a balance of the different properties assessed. Absorbance measurements at the peak excitation and emission wavelengths for the reporter fluorophores indicate that formulations with AAm/MBAm ratios of 15, 17.5, or 20 had the highest transmittance. Assessments of mechanical properties demonstrate that all polyacrylamide compositions tested yielded sufficient strength to penetrate the stratum corneum, whereas formulations with higher %AAm showed reduced shrinkage. Thus, a polyacrylamide composition of 30% AAm and AAm/MBAm ratio of 15 was selected due to the high optical transmission at the desired wavelengths, good mechanical strength, and minimal shrinkage percentage. Finally, we demonstrated porosity of this polymer composition, using fluorescence recovery after photo bleaching, to 2-NBDG, a commercially available fluorescent analog of glucose (which is a small molecule as phenylalanine, our test analyte). The diffusivity was measured as 5.7 ± 1.9 $\mu m^2/s$. Table 1 summarizes the properties of this polyacrylamide composition.

Assessment of Sensor Functionality in Hydrated Hydrogel

In our platform, the aptamer sensing moiety can be conjugated to microfilaments to enable passive *in situ* sensing, thereby bypassing delayed, complex, and potentially error-prone procedures that extract the interstitial fluid out of a microneedle onto an external electrochemical sensor. Here, we assessed whether a fluorescent aptamer sensor selected against phenylalanine can be covalently conjugated to the polyacrylamide matrix via co-polymerization and that the functionality is retained. The aptamer sensor (Figure 3A, inset) is composed of phenylalanine binding site, FAM and TAMRA fluorophore reporting unit, and an Acrydite handle to enable immobilization to the polyacrylamide matrix. As a future application, monitoring of phenylalanine is critical for patients with phenylketonuria, a genetic disease that leads to elevated phenylalanine levels, growth failure, and mental health disorders (Brumm et al., 2010; Williams et al., 2008). This sensor was selected as a model moiety, as aptamers are a flexible class of sensor that can be selected for a wide variety of target analytes (Ilgu and Nilsen-Hamilton, 2016) and easily functionalized to enable attachment. To demonstrate that the sensor functionality is maintained following conjugation to the hydrogel, hydrated hydrogel disks were exposed to solutions with different concentrations of phenylalanine.

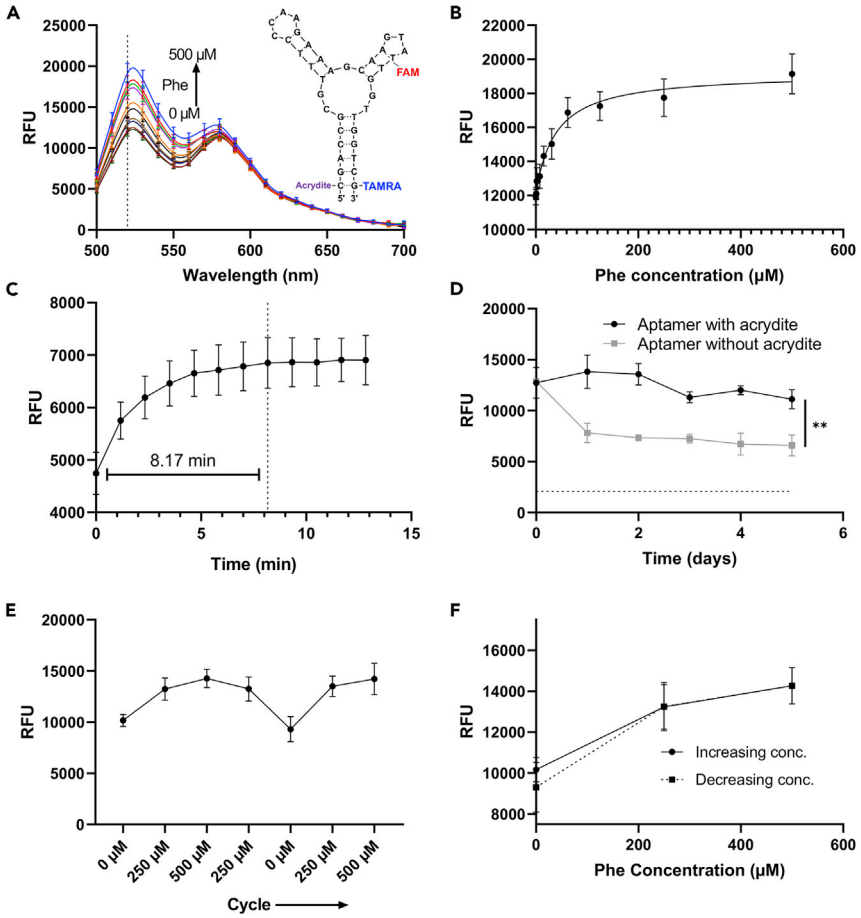

Figure 3. Sensor Performance Following Tethering to Hydrated Hydrogel [30% AAm 15, AAm/MBAm]

(A) Fluorescence emission spectra of hydrated hydrogel exposed to different concentration of phenylalanine solution and excitation at λ = 470 nm (n = 8). Inset shows the schematic of phenylalanine-responsive fluorescent aptamer sensor.

(B) Fluorescence intensity concentration response for hydrated hydrogel with excitation λ = 470 nm and emission λ = 520 nm (n = 8). The curve was fit using a Padé approximant.

(C) Response time for hydrated hydrogel after addition of 500 µM phenylalanine solution (n = 8).

(D) Fluorescence intensity for hydrated hydrogel disks with excitation λ = 470 nm and emission λ = 520 nm after soaking in PBS for 5 days with PBS changed daily. Hydrogel disks were fabricated using aptamer with or without the 5′-acrydite modification. The dotted line indicates the average fluorescence for a hydrated hydrogel disk with no aptamer (n = 3). Data analyzed using two-tailed t test. "**" indicates significant at $p < 0.01$.

(E) Fluorescence intensity for hydrated hydrogel with excitation λ = 470 nm and emission λ = 520 nm after cycling through different concentrations of phenylalanine (n = 3).

(F) Hysteresis loop showing the fluorescence intensity for hydrated hydrogel with excitation λ = 470 nm and emission λ = 520 nm after increasing and decreasing phenylalanine concentration (n = 3).

Data are represented as mean ± standard deviation. See also Figures S3–S5.

Figure 3A shows the fluorescence emission spectra of the hydrogel following excitation at 470 nm. The fluorescence peak intensity at 520 nm increased as the phenylalanine concentration increased from 0.0 to 500 µM (Figure 3B). Comparison to the emission spectra (Figure S3A) and fluorescence intensity at 520 nm (Figure S3B) for the aqueous sensor shows that the phenylalanine concentration dependence is maintained following chemical tethering to the polyacrylamide matrix. Disks were used instead of the microfilaments because the geometry was less fragile and could withstand the multiple read and wash cycles without breaking.

Real-time *in situ* sensing requires the sensor to quickly respond to the changing environment. The response time for the aqueous sensor is less than 20 s (Figure S4), indicating rapid response to changes in

phenylalanine concentration. The response time for the hydrogel-conjugated sensor is approximately 8 min for a disk approximately 6.4 mm in diameter and 1 mm in height (Figure 3C). As the dimensions for the microfilaments are up to an order of magnitude smaller than the disk, facilitating more rapid diffusion of the analyte through the hydrogel, we expect the response time for the microfilament array to be less than 8 min. Extended sensing requires that the aptamer be covalently attached to the polyacrylamide matrix such that the sensor does not diffuse out of the microfilaments, resulting in an erroneous decrease in fluorescence signal. To demonstrate this chemical tethering, sensor-laden polyacrylamide disks were fabricated, and the fluorescence intensity at 520 nm was tracked over 5 days where the disks were soaked in clean PBS buffer with the buffer replaced daily (Figure 3D). For hydrogel disks fabricated using aptamer without a 5′-acrydite modification, the fluorescence intensity decreased significantly within a day ($p < 0.01$) after soaking in buffer, likely due to diffusion of unconjugated sensor out of the gel. After this initial drop, the fluorescence intensity remains relatively constant and is greater than that for disks made without aptamer, indicating that some sensor may be physically encapsulated by the hydrogel matrix. For disks made with the 5′-acrydite modification, the fluorescence intensity remains relatively stable for the entire measurement period, indicative of successful tethering to the hydrogel.

Additionally, *in situ* sensing requires the sensor be reversible. To demonstrate reversible sensing, hydrogel disks were exposed to phenylalanine solutions with both increasing and decreasing concentration and the fluorescence intensity at 520 nm was recorded (Figure 3E). These data show that the phenylalanine aptamer sensor demonstrates reversible sensing, as an increase in phenylalanine concentration results in an increase in fluorescence intensity, whereas a decrease in concentration results in a subsequent decrease in intensity. The hysteresis loop for this reversible sensing (Figure 3F) shows that the sensor has minimal hysteresis. However, the aptamer sensor is susceptible to photobleaching (Figure S5), which may limit the duration of *in situ* sensing for a single microfilament array. (In the future, it may be possible to normalize for the effects of photobleaching, or monitor at 520 and 580 nm for ratiometric sensing, which is less sensitive to effects of photobleaching.)

Exploration of Design of Microfilament Array for Low Human Pain

Toward the goal of eliciting minimal pain on the user, we note that previous studies that studied microneedles and human pain sensation (Gill et al., 2008; Haq et al., 2009; Park et al., 2007) have demonstrated the predominant factors to be length of needle, and secondarily, number of needles, diameter, and sharpness. As such, previous studies (Gill et al., 2008; Haq et al., 2009) have investigated different geometric design parameters of the microneedle array (number of microneedles in array and needle height and diameter) on human pain assessments, but typically each parameter was investigated independently of the others, with compound effects unexplored. Here, we performed a human pain assessment using microneedles fabricated from polyether ether ketone (PEEK), which is FDA approved for experiments on human subjects and can be easily steam sterilized. (We measured the Young's modulus of PEEK to be 4.3 ± 0.2 GPa, within an order of magnitude, but even higher, of that of the dehydrated hydrogel; both the PEEK microneedles and hydrogel microfilaments are sufficiently stiff to avoid bending-induced fracture (Zahn et al., 2000).) We machined PEEK microneedles to identify geometric parameters that elicited low human pain and subsequently fabricated dehydrated polyacrylamide microfilaments with matching length, number of filaments in array, diameter, and bevel.

First, we recruited human subjects to assess pain levels induced by insertion of microneedles compared with pressing the hook surface of a hook-and-loop fastener (Velcro) against the skin. The raw visual analog scale (VAS) pain scores (Hawker et al., 2011) (Figure 4A, top left) and those normalized to a 26-guage hypodermic needle (Figure S6A) from 15 human subjects showed that the sensation experienced by the insertion of a 3 × 3 PEEK microneedle array with needles of 200 μm diameter and 1,400 μm height induced slightly more pain compared with a press of the Velcro patch against the skin but is still significantly less painful ($p < 0.0001$) compared with a standard 26-gauge hypodermic needle. (Qualitative feedback from human subjects also indicated there was minimal discomfort after insertion of device.)

We tested insertion of arrays with 1, 4, or 9 microneedles arranged in a 1 × 1, 2 × 2, or 3 × 3 grid, respectively, keeping constant the diameter (200 μm), height (1400 μm), and bevel (74°). Raw (Figure 4A, top right) and normalized (Figure S6B) VAS pain scores indicated that the number of microneedles in an array did not significantly affect pain. Thus, we selected an array with 9 gel microfilaments in order to maximize the fluorescent signal. We also tested insertion of 3 × 3 arrays with needles of 200 μm diameter, while varying the

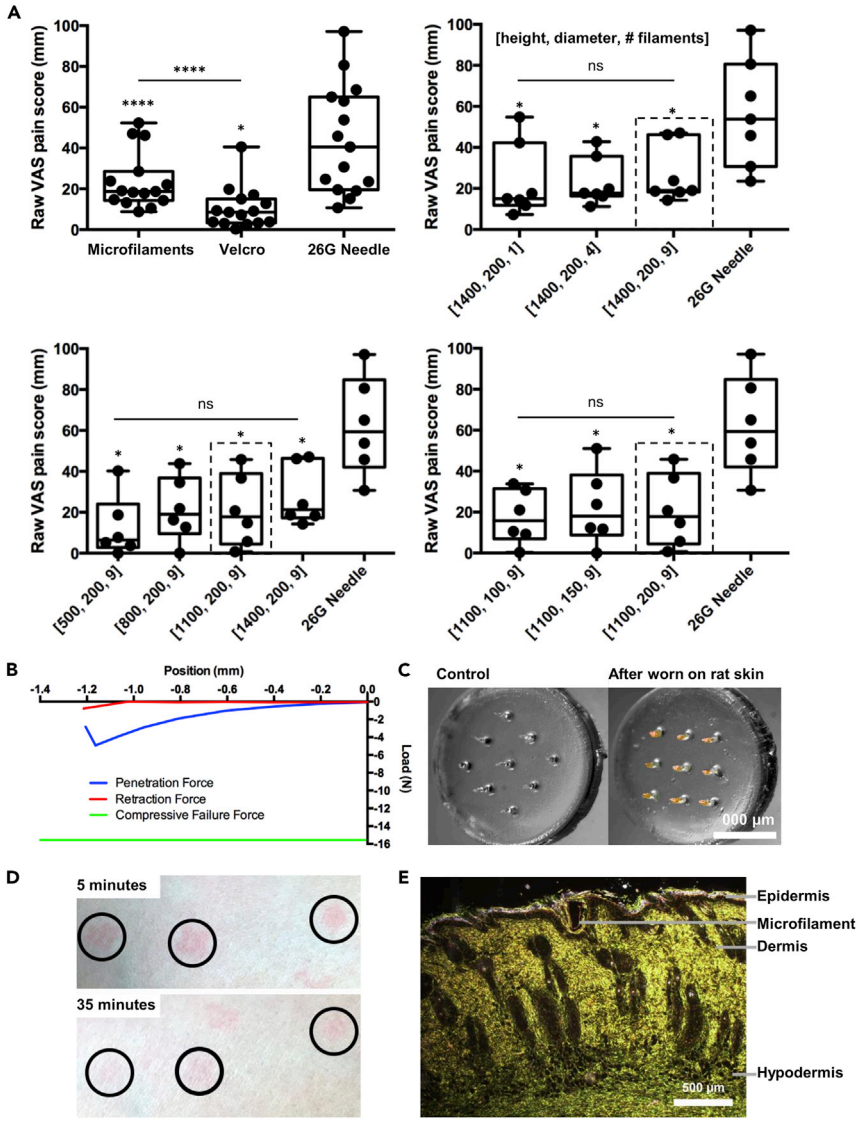

Figure 4. Exploration of Microfilament Array Design and Assessment of Skin Penetration and Healing

(A) Box plots of raw VAS pain scores after insertion of microfilament arrays with varying geometries. The dotted lines indicate the design that was identified as optimal for each group. Top left: 3 × 3 array of microfilaments with 200 µm diameter and 1,400 µm height microfilaments, application of a Velcro patch to the skin, or insertion of a 26-guage hypodermic needle (n = 15). Top right: microfilament array with 1, 4, or 9 microfilaments of 200 µm diameter and 1,400 µm height or insertion of a 26-guage hypodermic needle (n = 7). Bottom left: 3 × 3 microfilament array with 200 µm diameter and 500–1400 µm height microfilaments or insertion of a 26-guage hypodermic needle (n = 6). Bottom right: a 3 × 3 microfilament array with 100–200 µm diameter and 1,100 µm height microfilaments or insertion of a 26-guage hypodermic needle (n = 6). Data analyzed using a one-way ANOVA with Sidak post-hoc test. "ns" indicates not significant, "*" indicates significant at $p < 0.05$, "****" indicates significant at $p < 0.0001$. Symbol above group indicates comparison with 26G Needle. Line indicates comparison between groups. See also Figure S6.

(B) Representative force-displacement curve during insertion into and removal of a 3 × 3 microfilament array from human cadaver skin. The bottom line marks the compressive force required to fracture desiccated microfilaments during insertion into the skin.

(C) Image of microfilament array worn on rat skin for 1 h and a control array not worn. Arrays were subsequently treated with silver nitrate to indicate exposure to chloride ions. For visualization purposes, the red and yellow channels were boosted for the control and experimental arrays to highlight the silver deposits.

(D) Image of microfilament array penetration site on the skin surface of a human subject 5 or 35 min after device removal. The insertion sites have been circled.

(E) Bright-field micrograph of rat skin histological section 24 h after insertion of microfilament platform.

height from 500 to 1,400 μm. The raw (Figure 4A, bottom left) and normalized (Figure S6C) VAS pain scores showed that, for the heights probed, microneedle height did not appreciably affect insertion pain, with no significant difference between 800 μm and 1,100 μm. Thus, to both maximize the fluorescent signal and minimize insertion pain, the design with a microfilament height of 1,100 μm was selected. Finally, insertion of 3 × 3 arrays with needle height of 1,100 μm and diameters ranging from 100 to 200 μm (Figures 4A, bottom right, S6D) showed an increase in the median pain score with increasing diameter, but the differences were not significant (as further confirmed by qualitative feedback from human subjects). Overall, we selected for the microfilament array to be a 3 × 3 array with microfilaments of 200 μm diameter and 1,100 μm height. Taking into account the shrinkage percentage of the chosen polyacrylamide formulation, this target geometry was achieved after desiccation of hydrated microfilaments of 300 μm diameter and 1,500 μm height.

Assessment of Skin Penetration and Healing

Finally, we performed a number of assessments to evaluate the ability of microfilaments to penetrate the skin and contact interstitial fluid. To assess the ability of the polyacrylamide microfilament sensor platform to penetrate the human skin without breaking and leaving polymer residues inside the skin, we measured the penetration and failure force. To measure the penetration force, we used human cadaver skin as a model (Wang et al., 2006; Park et al., 2005). Full-thickness human cadaver skin was mounted on the base platen of a material testing machine equipped with a 25-lb load cell. The microfilament array was affixed to the upper platen of the mechanical tester. The array was brought into contact with the tissue, and the force for insertion was recorded. The array was then displaced in the opposite direction, and the force for removal was recorded. Mechanical failure was considered due to axial loading. Comparison of the force required to penetrate the polyacrylamide microfilaments into human cadaver skin and the force required to fracture the microfilaments, Figure 4B, demonstrates that the microfilaments provide sufficient mechanical strength to penetrate the human skin without breaking and leaving residues inside the skin. The force required to penetrate a 3 × 3 array of microfilaments into human skin is around 5 N, whereas the compressive failure force is approximately 16 N (corresponding to a compressive strength on the order of hundreds of MPa).

To demonstrate the ability of polyacrylamide microfilaments to penetrate the stratum corneum and contact dermal interstitial fluid, we applied microfilaments on the skin of live, anesthetized hairless rats. We gently pressed the microfilament arrays into the skin, secured it in position with a skin adhesive, and after one hour, removed the microfilament array and treated it with silver nitrate to detect for the presence of chloride ions from dermal interstitial fluid. Figure 4C shows localization of silver deposits to the microfilament shafts, whereas the control array, not applied to rat skin, does not indicate the presence of chloride ions. The presence of silver deposits and their localization to the shafts of the microfilaments demonstrate that chloride ions were sampled not from the superficial layer of the skin, but rather from the interstitial fluid beneath the epidermis.

To assess the healing response of the human skin after insertion and removal of PEEK microfilament arrays, we captured images of the human skin surface after device removal. Figure 4D shows images of the microfilament array penetration sites on the skin of a human subject at 5 and 35 min after device removal. The faint redness on most of the penetration sites, indicating minimal inflammation, subsided within 2 h after removal of device. (As PEEK is biocompatible and the arrays were inserted for only ~10 s, the observed inflammation was likely due to mechanical trauma and would likely be similar for a gel polyacrylamide array with the same length, number, diameter, and sharpness of filaments.) Finally, histological samples of polyacrylamide microfilament insertion sites on rat skin were obtained to examine the wound healing response *in vivo*. Figure 4E shows a histological image at a microfilament insertion site, with a microfilament still embedded within, further confirming that polyacrylamide microfilaments penetrated the epidermis to contact the dermal layer. With regard to the wound healing response in an *in vivo* model, over 24 h post application, the epidermis reformed and engulfed around the microfilament, indicative of fast healing of the puncture site. As expected from the small dimensions of microfilaments, the puncture site was observed to rapidly reseal.

Steps toward Translation

To translate the proposed system to the clinic, a number of challenges must be considered. For manufacturing, the demonstrated fabrication method can be scaled up by increasing the batch size

(e.g. using larger molds with more arrays and curing in a UV oven) and automating the fabrication. Sterilization of the mold and polymer precursor solution can potentially be achieved by UV germicidal irradiation (Huebsch et al., 2005). Relating to the use of the platform, the patch is intended to be worn over the length of the desired measurement period, until the performance of the sensor has degraded due to photobleaching or until discomfort. To facilitate safe and reproducible insertion of the device, a simple applicator device could be designed in the future to apply the suitable force to penetrate the skin. Because the microfilaments are sufficiently stiff to avoid bending-induced fracture, we do not expect fragments of the microfilaments to be deposited into the skin; any small fragments lodged inside the skin, after removing the device, would reside primarily in the epidermis and be expected to be discarded via regular skin turnover within 2–4 weeks (S. Leo et al., 2014). During the manufacturing process, the microfilaments should be thoroughly washed after polymerization to remove unconjugated aptamers; aptamers covalently attached to the hydrogel are not expected to leach into the skin. Toward the goal of extended use, the effects of sweat and bathing on the performance of the system should be studied, as well as any potential immune response (although polyacrylamide (Hadjesfandiari and Parambath, 2018) and aptamers (Zhou and Rossi, 2017) have been demonstrated as non-immunogenic). Finally, the response time *in vivo* should be studied to take into account the time needed for interstitial fluid to diffuse through the microfilaments (which we currently estimate would be several minutes *in vivo*).

Beyond the continuous *in situ* monitoring in humans, a microfilament platform fabricated out of biocompatible hydrogel can be used for minimally invasive collection of interstitial fluid for downstream discrete analysis (similar to minimally invasive one-step blood-collection devices (Blicharz et al., 2018)), as the interstitial fluid sample resides within the microfilaments. Alternatively, the device could be adapted for monitoring chemical analytes in animal models to support basic science. As dermal interstitial fluid is rich with potential target analytes, the hydrogel microfilament platform could be adapted to monitor a wide variety of analytes, including electrolytes, saccharides, hormones, lactate, amino acids, proteins, enzymes, co-enzymes, triglycerides, oxygen, creatinine, urea, and reactive oxygen and nitrogen species (Ruckh and Clark, 2014; Paliwal et al., 2013).

Conclusion

In this work, we reported a microfilament platform fabricated from polyacrylamide hydrogel conjugated with phenylalanine aptamer sensor with fluorescence readout. To enable penetration of the stratum corneum, the microfilament platform was designed to be sharp and stiff. By optimizing the polymer formulation via %AAm and AAm/MBAm ratio, we were able to fabricate polyacrylamide hydrogel microfilament arrays with a sharp 5-bevel tip that was maintained after desiccation. Further, the desiccated microfilaments exhibited high mechanical strength with the compressive failure force exceeding both the force of insertion and removal. When rehydrated, the hydrogel demonstrated good transmittance at the desired wavelengths, and the functionality of a phenylalanine aptamer sensor attached via co-polymerization was preserved. The design of the microfilament array was optimized to minimize pain during insertion while maximizing the volume of the analyte-responsive microfilaments to thereby maximize fluorescence signal. The implemented microfilament design exhibited less insertion pain than a hypodermic needle and was more comparable to a piece of Velcro. Although the functionality of only one sensor was demonstrated, the microfilament platform can be adapted for alternative analytes by incorporating other sensors functionalized with acrylamide copolymers. This work points a path forward for using hydrogel microfilaments as skin patch continuous sensors without requiring surgery.

Limitations of the Study

The main limitation of this study is the lack of validation of a fully integrated system, which would include characterization of sensor performance from the microfilaments in an *in vivo* animal model. Considerable work has been done on portable fluorometer development (Alam et al., 2019; Kostov et al., 2014), such that in future studies, one of these designs could be adapted to interface with the platform presented. In addition, systematic studies of pore sizes for different polymer formulations, as well as tuning the formulation to accommodate sensing of different analytes (i.e. such that the Stokes radius of the analyte is less than 10% compared with the polyacrylamide pore radius (Deen et al., 1981)) could be performed. Finally, we have only demonstrated incorporation of a single sensor. However, aptamers can be selected for many different targets with chemistry similar to the utilized moiety. Thus, we anticipate alternative sensors could be incorporated without loss of functionality.

METHODS

All methods can be found in the accompanying Transparent Methods supplemental file.

SUPPLEMENTAL INFORMATION

Supplemental Information can be found online at https://doi.org/10.1016/j.isci.2019.10.036.

ACKNOWLEDGMENTS

We thank Tyler J. Poore and Willem J. Prins. This work was supported in part by grants from the National Institutes of Health (1R01DA045550) and the National Science Foundation (Graduate Research Fellowship under Grant No. DGE 1644869).

AUTHOR CONTRIBUTIONS

N.T. and S.S. conceptualized the project. S.S. supervised the project. N.T. and D.C. designed experiments and analyzed data. N.T., D.C., F.M., V.G., and S.C. performed experiments. K.Y. designed and tested aptameric sensor candidates. K.Y. and M.S. provided materials. N.T. drafted a manuscript, and D.C. and S.S. wrote the manuscript.

DECLARATION OF INTERESTS

A patent based on these results has been filed by Columbia University.

Received: July 19, 2019
Revised: October 3, 2019
Accepted: October 18, 2019
Published: November 22, 2019

REFERENCES

Alam, M.W., Wahid, K.A., Goel, R.K., and Lukong, K.E. (2019). Development of a low-cost and portable smart fluorometer for detecting breast cancer cells. Biomed. Opt. Express *10*, 399–410.

Alizadeh, A., Burns, A., Lenigk, R., Gettings, R., Ashe, J., Porter, A., Mccaul, M., Barrett, R., Diamond, D., White, P., et al. (2018). A wearable patch for continuous monitoring of sweat electrolytes during exertion. Lab Chip *18*, 2632–2641.

Bansil, R., and Gupta, M.K. (1980). Effect of varying crosslinking density on polyacrylamide gels. Ferroelectrics *30*, 63–71.

Barrett, C., Dawson, K., O'mahony, C., and O'riordan, A. (2015). Development of low cost rapid fabrication of sharp polymer microneedles for in vivo glucose biosensing applications. ECS J Solid State Sci Technol. *4*, S3053–S3058.

Blicharz, T.M., Gong, P., Bunner, B.M., Chu, L.L., Leonard, K.M., Wakefield, J.A., Williams, R.E., Dadgar, M., Tagliabue, C.A., El Khaja, R., et al. (2018). Microneedle-based device for the one-step painless collection of capillary blood samples. Nat. Biomed. Eng. *2*, 151–157.

Brumm, V.L., Bilder, D., and Waisbren, S.E. (2010). Psychiatric symptoms and disorders in phenylketonuria. Mol. Genet. Metab *99* (*Suppl 1*), S59–S63.

Caffarel-Salvador, E., Brady, A.J., Eltayib, E., Meng, T., Alonso-Vicente, A., Gonzalez-Vazquez, P., Torrisi, B.M., Vicente-Perez, E.M., Mooney, K., Jones, D.S., et al. (2015). Hydrogel-forming microneedle arrays allow detection of drugs and glucose in vivo: potential for use in diagnosis and therapeutic drug monitoring. PLoS One *10*, e0145644.

Chen, X.F., Prow, T.W., Crichton, M.L., Jenkins, D.W.K., Roberts, M.S., Frazer, I.H., Fernando, G.J.P., and Kendall, M.A.F. (2009). Dry-coated microprojection array patches for targeted delivery of immunotherapeutics to the skin. J. Control. Release *139*, 212–220.

Chien, J.S., Mohammed, M., Eldik, H., Ibrahim, M.M., Martinez, J., Nichols, S.P., Wisniewski, N., and Klitzman, B. (2017). Injectable phosphorescence-based oxygen biosensors identify post ischemic reactive hyperoxia. Sci. Rep. *7*, 8255.

Crompton, T.R. (2012). 1-Mechanical properties of polymers. In Physical Testing of Plastics (Smithers Rapra Technology), pp. 1–148.

Currano, L.J., Sage, F.C., Hagedon, M., Hamilton, L., Patrone, J., and Gerasopoulos, K. (2018). Wearable sensor system for detection of lactate in sweat. Sci. Rep. *8*, 15890.

Deen, W.M., Bohrer, M.P., and Epstein, N.B. (1981). Effects of molecular-size and configuration on diffusion in microporous membranes. Aiche J. *27*, 952–959.

Denisin, A.K., and Pruitt, B.L. (2016). Tuning the range of polyacrylamide gel stiffness for mechanobiology applications. ACS Appl. Mater. Interfaces *8*, 21893–21902.

Forlenza, G.P., Argento, N.B., and Laffel, L.M. (2017). Practical considerations on the use of continuous glucose monitoring in pediatrics and older adults and nonadjunctive use. Diabetes Technol. Ther. *19*, S13–S20.

Gill, H.S., Denson, D.D., Burris, B.A., and Prausnitz, M.R. (2008). Effect of microneedle design on pain in human volunteers. Clin. J. Pain *24*, 585–594.

Guckenberger, D.J., De Groot, T.E., Wan, A.M.D., Beebe, D.J., and Young, E.W.K. (2015). Micromilling: a method for ultra-rapid prototyping of plastic microfluidic devices. Lab Chip *15*, 2364–2378.

Hadjesfandiari, N., and Parambath, A. (2018). 13-Stealth coatings for nanoparticles: polyethylene glycol alternatives. In Engineering of Biomaterials for Drug Delivery Systems, A. Parambath, ed. (Woodhead Publishing), pp. 345–361.

Haq, M.I., Smith, E., John, D.N., Kalavala, M., Edwards, C., Anstey, A., Morrissey, A., and Birchall, J.C. (2009). Clinical administration of microneedles: skin puncture, pain and sensation. Biomed. Microdevices *11*, 35–47.

Hawker, G.A., Mian, S., Kendzerska, T., and French, M. (2011). Measures of adult pain visual analog scale for pain (VAS pain), numeric rating scale for pain (NRS pain), McGill pain questionnaire (MPQ), short-form McGill pain questionnaire (SF-MPQ), chronic pain grade scale (CPGS), short form-36 bodily pain scale (SF-36 BPS), and measure of intermittent and constant osteoarthritis pain (ICOAP). Arthritis Care Res. *63*, S240–S252.

Hirsch, L., Gibney, M., Berube, J., and Manocchio, J. (2012). Impact of a modified needle tip geometry on penetration force as well as acceptability, preference, and perceived pain in subjects with diabetes. J. Diabetes Sci. Technol. *6*, 328–335.

Holmes, D.L., and Stellwagen, N.C. (1991). Estimation of polyacrylamide-gel pore-size from ferguson plots of linear DNA fragments .2. Comparison of gels with different cross-linker concentrations, added agarose and added linear polyacrylamide. Electrophoresis *12*, 612–619.

Huebsch, N., Gilbert, M., and Healy, K.E. (2005). Analysis of sterilization protocols for peptide-modified hydrogels. J. Biomed. Mater. Res. B Appl. Biomater. *74b*, 440–447.

Ilgu, M., and Nilsen-Hamilton, M. (2016). Aptamers in analytics. Analyst *141*, 1551–1568.

Invernale, M.A., Tang, B.C., York, R.L., Le, L., Hou, D.Y., and Anderson, D.G. (2014). Microneedle electrodes toward an amperometric glucose-sensing smart patch. Adv. Healthc. Mater. *3*, 338–342.

Ito, Y., Hirono, M., Fukushima, K., Sugioka, N., and Takada, K. (2012). Two-layered dissolving microneedles formulated with intermediate-acting insulin. Int. J. Pharmaceutics *436*, 387–393.

Jina, A., Tierney, M.J., Tamada, J.A., Mcgill, S., Desai, S., Chua, B., Chang, A., and Christiansen, M. (2014). Design, development, and evaluation of a novel microneedle array-based continuous glucose monitor. J. Diabetes Sci. Technol. *8*, 483–487.

Johnston, I.D., Mccluskey, D.K., Tan, C.K.L., and Tracey, M.C. (2014). Mechanical characterization of bulk Sylgard 184 for microfluidics and microengineering. J. Micromech. Microeng. *24*, 035017.

Le Goff, G.C., Srinivas, R.L., Hill, W.A., and Doyle, P.S. (2015). Hydrogel microparticles for biosensing. Eur. Polym. J. *72*, 386–412.

Kanick, S.C., Schneider, P.A., Klitzman, B., Wisniewski, N.A., and Rebrin, K. (2019). Continuous monitoring of interstitial tissue oxygen using subcutaneous oxygen microsensors: in vivo characterization in healthy volunteers. Microvasc. Res. *124*, 6–18.

Kiang, T.K.L., Ranamukhaarachchi, S.A., and Ensom, M.H.H. (2017). Revolutionizing therapeutic drug monitoring with the use of interstitial fluid and microneedles technology. Pharmaceutics *9*, 43.

Kostov, Y., Ge, X.D., Rao, G., and Tolosa, L. (2014). Portable system for the detection of micromolar concentrations of glucose. Meas. Sci. Technol. *25*, 025701.

Lei, B.U.W., and Prow, T.W. (2019). A review of microsampling techniques and their social impact. Biomed. Microdevices *21*, 81.

Leo, M.S., Lev-Tov, H.A., Kamangar, F., Maibach, H., and Sivamani, R. (2014). Efficacy and Toxicity of Microneedle-Based Devices. In Topical Drug Bioavailability, Bioequivalence, and Penetration, V. Shah, H. Maibach, and J. Jenner, eds. (New York: Springer-Verlag).

Li, T., Barnett, A., Rogers, K.L., and Gianchandani, Y.B. (2009). A blood sampling microsystem for pharmacokinetic applications: design, fabrication, and initial results. Lab Chip *9*, 3495–3503.

Li, C.G., Lee, C.Y., Lee, K., and Jung, H. (2013). An optimized hollow microneedle for minimally invasive blood extraction. Biomed. Microdevices *15*, 17–25.

Li, Y., Young, D.J., and Loh, X.J. (2019). Fluorescent gels: a review of synthesis, properties, applications and challenges. Mater. Chem. Front. *3*, 1489–1502.

Liang, X., and Boppart, S.A. (2010). Biomechanical properties of in vivo human skin from dynamic optical coherence elastography. IEEE Trans. Biomed. Eng. *57*, 953–959.

Mcvey, E., Sutter, D., Rini, C., Nosek, L., Kapitza, C., Rebrin, K., and Pettis, R. (2014). Intradermal insulin infusion achieves faster insulin action than subcutaneous infusion for three day wear. Diabetes Technol. Ther. *16*, A27–A28.

Mukerjee, E., Collins, S.D., Isseroff, R.R., and Smith, R.L. (2004). Microneedle array for transdermal biological fluid extraction and in situ analysis. Sens. Actuators A Phys. *114*, 267–275.

Nicolson, P.C., and Vogt, J. (2001). Soft contact lens polymers: an evolution. Biomaterials *22*, 3273–3283.

Nyein, H.Y.Y., Tai, L.C., Ngo, Q.P., Chao, M., Zhang, G.B., Gao, W., Bariya, M., Bullock, J., Kim, H., Fahad, H.M., and Javey, A. (2018). A wearable microfluidic sensing patch for dynamic sweat secretion analysis. ACS Sens. *3*, 944–952.

Paliwal, S., Hwang, B.H., Tsai, K.Y., and Mitragotri, S. (2013). Diagnostic opportunities based on skin biomarkers. Eur. J. Pharm. Sci. *50*, 546–556.

Park, H.I., and Park, S.Y. (2018). Smart fluorescent hydrogel glucose biosensing microdroplets with dual-mode fluorescence quenching and size reduction. Acs Appl. Mater. Interfaces *10*, 30172–30179.

Park, J.H., and Prausnitz, M.R. (2010). Analysis of the mechanical failure of polymer microneedles by axial force. J. Korean Phys. Soc. *56*, 1223–1227.

Park, J.H., Allen, M.G., and Prausnitz, M.R. (2005). Biodegradable polymer microneedles: fabrication, mechanics and transdermal drug delivery. J. Controll. Release *104*, 51–66.

Park, J.H., Yoon, Y.K., Choi, S.O., Prausnitz, M.R., and Allen, M.G. (2007). Tapered conical polymer microneedles fabricated using an integrated lens technique for transdermal drug delivery. IEEE Trans. Biomed. Eng. *54*, 903–913.

Parlak, O., Keene, S.T., Marais, A., Curto, V.F., and Salleo, A. (2018). Molecularly selective nanoporous membrane-based wearable organic electrochemical device for noninvasive cortisol sensing. Sci. Adv. *4*, eaar2904.

Ramchandani, N., Arya, S., Ten, S., and Bhandari, S. (2011). Real-life utilization of real-time continuous glucose monitoring: the complete picture. J. Diabetes Sci. Technol. *5*, 860–870.

Ruckh, T.T., and Clark, H.A. (2014). Implantable nanosensors: toward continuous physiologic monitoring. Anal. Chem. *86*, 1314–1323.

Slattery, D., and Choudhary, P. (2017). Clinical use of continuous glucose monitoring in adults with type 1 diabetes. Diabetes Technol. Ther. *19*, S55–S61.

Stieglitz, T., and Schuettler, M. (2013). 2-Material–tissue interfaces in implantable systems. In Implantable Sensor Systems for Medical Applications, A. Inmann and D. Hodgins, eds. (Woodhead Publishing), pp. 39–67.

Sullivan, S.P., Koutsonanos, D.G., Martin, M.D., Lee, J.W., Zarnitsyn, V., Choi, S.O., Murthy, N., Compans, R.W., Skountzou, I., and Prausnitz, M.R. (2010). Dissolving polymer microneedle patches for influenza vaccination. Nat. Med. *16*, 915–920.

Tan, B., Zhao, H.M., Du, L., Gan, X.R., and Quan, X. (2016). A versatile fluorescent biosensor based on target-responsive graphene oxide hydrogel for antibiotic detection. Biosens. Bioelectron. *83*, 267–273.

Toozs-Hobson, P., Al-Singary, W., Fynes, M., Tegerstedt, G., and Lose, G. (2012). Two-year follow-up of an open-label multicenter study of polyacrylamide hydrogel (Bulkamid(R)) for female stress and stress-predominant mixed incontinence. Int. Urogynecol. J. *23*, 1373–1378.

Wang, P.M., Cornwell, M., and Prausnitz, M.R. (2005). Minimally invasive extraction of dermal interstitial fluid for glucose monitoring using microneedles. Diabetes Technol. Ther. *7*, 131–141.

Tsuchiya, K., Isobata, K., Sato, M., Uetsuji, Y., Nakamachi, E., Kajiwara, K., and Kimura, M. (2007). Design of painless microneedle for blood extraction system. Biomems Nanotechnology III *6799*.

Wang, P.M., Cornwell, M., Hill, J., and Prausnitz, M.R. (2006). Precise microinjection into skin using hollow microneedles. J. Invest. Dermatol. *126*, 1080–1087.

Welsh, J.B., Gao, P., Derdzinski, M., Puhr, S., Johnson, T.K., Walker, T.C., and Graham, C. (2019a). Accuracy, utilization, and effectiveness comparisons of different continuous glucose monitoring systems. Diabetes Technol. Ther. *21*, 128–132.

Welsh, J.B., Zhang, X., Puhr, S.A., Johnson, T.K., Walker, T.C., Balo, A.K., and Price, D. (2019b). Performance of a factory-calibrated, real-time continuous glucose monitoring system in pediatric participants with type 1 diabetes. J. Diabetes Sci. Technol. *13*, 254–258.

Williams, R.A., Mamotte, C.D., and Burnett, J.R. (2008). Phenylketonuria: an inborn error of phenylalanine metabolism. Clin. Biochem. Rev. *29*, 31–41.

Windmiller, J.R., Zhou, N.D., Chuang, M.C., Valdes-Ramirez, G., Santhosh, P., Miller, P.R., Narayan, R., and Wang, J. (2011). Microneedle array-based carbon paste amperometric sensors and biosensors. Analyst *136*, 1846–1851.

Yan, G.A., Warner, K.S., Zhang, J., Sharma, S., and Gale, B.K. (2010). Evaluation needle length and density of microneedle arrays in the pretreatment

of skin for transdermal drug delivery. Int. J. Pharmaceutics *391*, 7–12.

Yang, S.Y., O'cearbhaill, E.D., Sisk, G.C., Park, K.M., Cho, W.K., Villiger, M., Bouma, B.E., Pomahac, B., and Karp, J.M. (2013). A bio-inspired swellable microneedle adhesive for mechanical interlocking with tissue. Nat. Commun. *4*, 1702.

Yu, J.C., Zhang, Y.Q., Ye, Y.Q., Disanto, R., Sun, W.J., Ranson, D., Ligler, F.S., Buse, J.B., and Gu, Z. (2015). Microneedle-array patches loaded with hypoxia-sensitive vesicles provide fast glucose-responsive insulin delivery. Proc. Natl. Acad. Sci. U S A *112*, 8260–8265.

Zahn, J.D., Talbot, N.H., Liepmann, D., and Pisano, A.P. (2000). Microfabricated polysilicon microneedles for minimally invasive biomedical devices. Biomed. Microdevices *2*, 295–303.

Zahn, J.D., Trebotich, D., and Liepmann, D. (2005). Microdialysis microneedles for continuous medical monitoring. Biomed. Microdevices *7*, 59–69.

Zhao, X.H. (2017). Designing toughness and strength for soft materials. Proc. Natl. Acad. Sci. U S A *114*, 8138–8140.

Zhou, J.H., and Rossi, J. (2017). Aptamers as targeted therapeutics: current potential and challenges. Nat. Rev. Drug Discov. *16*, 181–202.

ISCI, Volume *21*

Supplemental Information

Hydrogel Microfilaments

toward Intradermal Health Monitoring

Nalin Tejavibulya, David A.M. Colburn, Francis A. Marcogliese, Kyung-Ae Yang, Vincent Guo, Shilpika Chowdhury, Milan N. Stojanovic, and Samuel K. Sia

Supplemental Figures

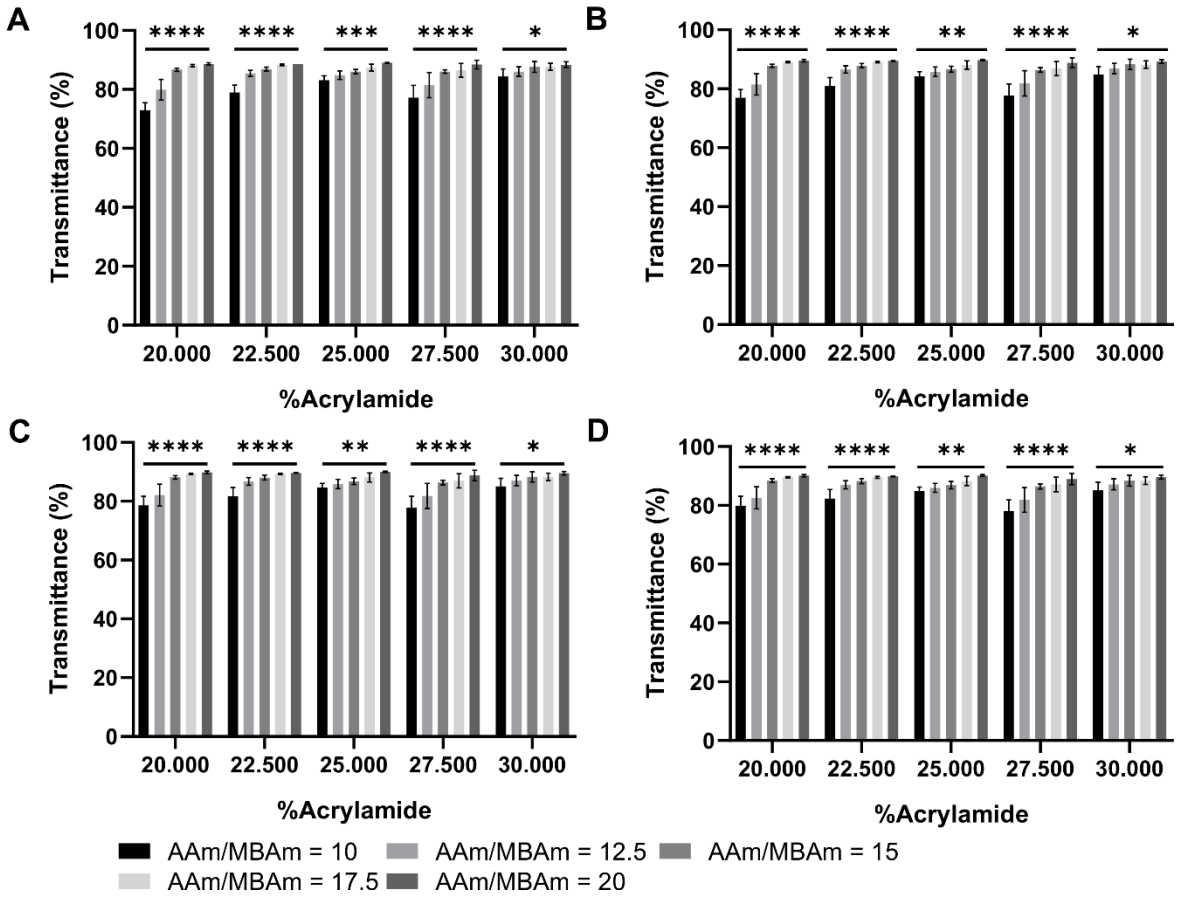

Figure S1. Percent transmittance of polyacrylamide hydrogel, related to Figure 2B. (A) Percent transmittance values of polyacrylamide disks at λ = 470 nm and (B) λ = 520 nm, the peak excitation and emission wavelengths for FAM, respectively (n=4). (C) Percent transmittance values of hydrated polyacrylamide disks at λ = 550 nm and (D) λ = 580 nm, the peak excitation and emission wavelengths for TAMRA, respectively (n=4). Data analyzed using a two-way ANOVA with Tukey post-hoc test. “ns” indicates not significant, “*” indicates significant at $p < 0.05$, “**” indicates significant at $p < 0.01$, “***” indicates significant at $p < 0.001$, and “****” indicates significant at $p < 0.0001$. Line indicates comparison between groups. Data are represented as mean ± standard deviation.

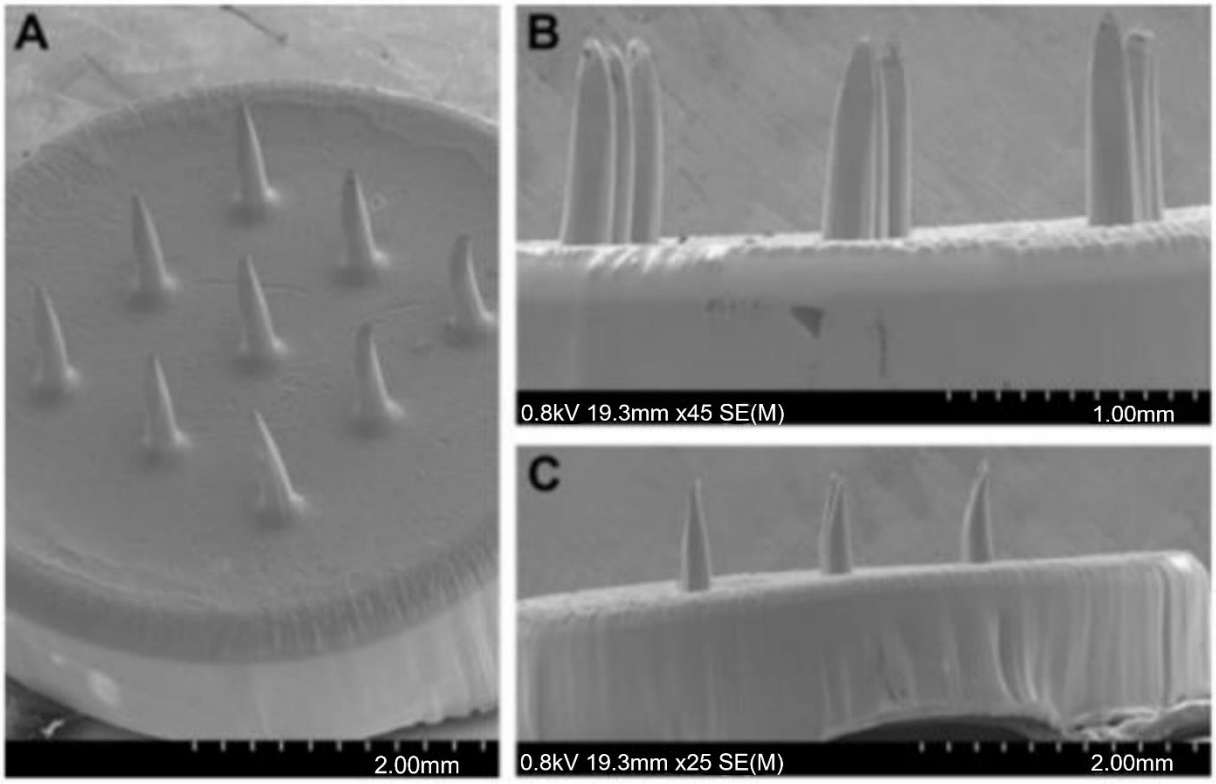

Figure S2. SEM images of microfilament array, related to Figure 2C. (A) Image at 45° relative to the base. (B) Image from the side with bevel facing forward. (C) Image from the side with bevel facing sideways.

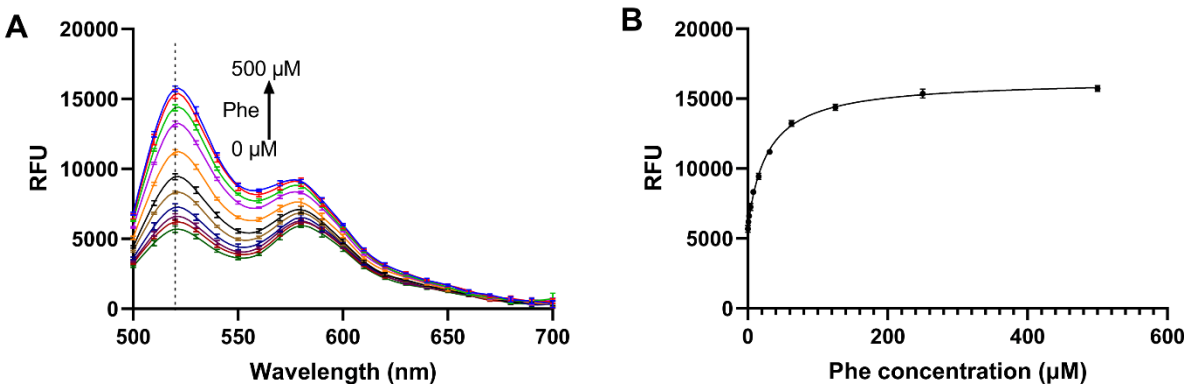

Figure S3. Concentration dependence of emission spectra and peak emission wavelength, related to Figure 3. (A) Fluorescence emission spectra of aqueous aptamer sensor exposed to different concentrations of phenylalanine solution and excited at λ = 470 nm (n=5). (B) Fluorescence intensity concentration response for aqueous aptamer sensor with excitation λ = 470 nm and emission λ = 520 nm (n=5). The curve was fit using a Padé approximant. Data are represented as mean ± standard deviation.

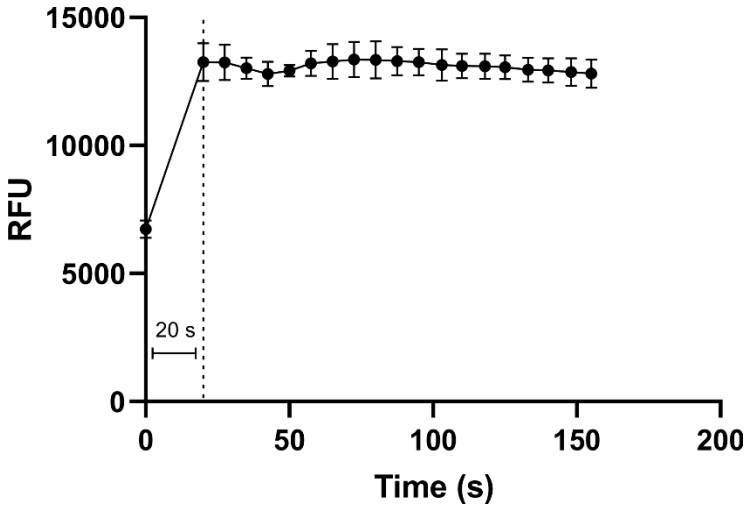

Figure S4. Response time of aqueous aptamer sensor, related to Figure 3. Fluorescence intensity for aqueous aptamer sensor with λ = 470 nm and emission λ = 520 nm after increasing phenylalanine concentration from 0 µM to 500 µM (n=3). Data are represented as mean ± standard deviation.

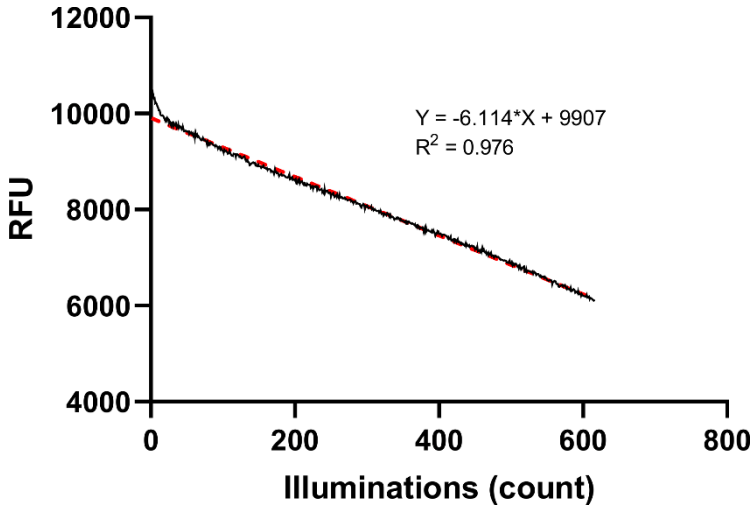

Figure S5. Photobleaching of aqueous aptamer sensor, related to Figure 3. Mean fluorescence intensity of aqueous aptamer sensor after repeated reads with excitation λ = 470 nm and emission λ = 520 nm (n=5). Red dotted line indicates the line of best fit. Data are represented as mean.

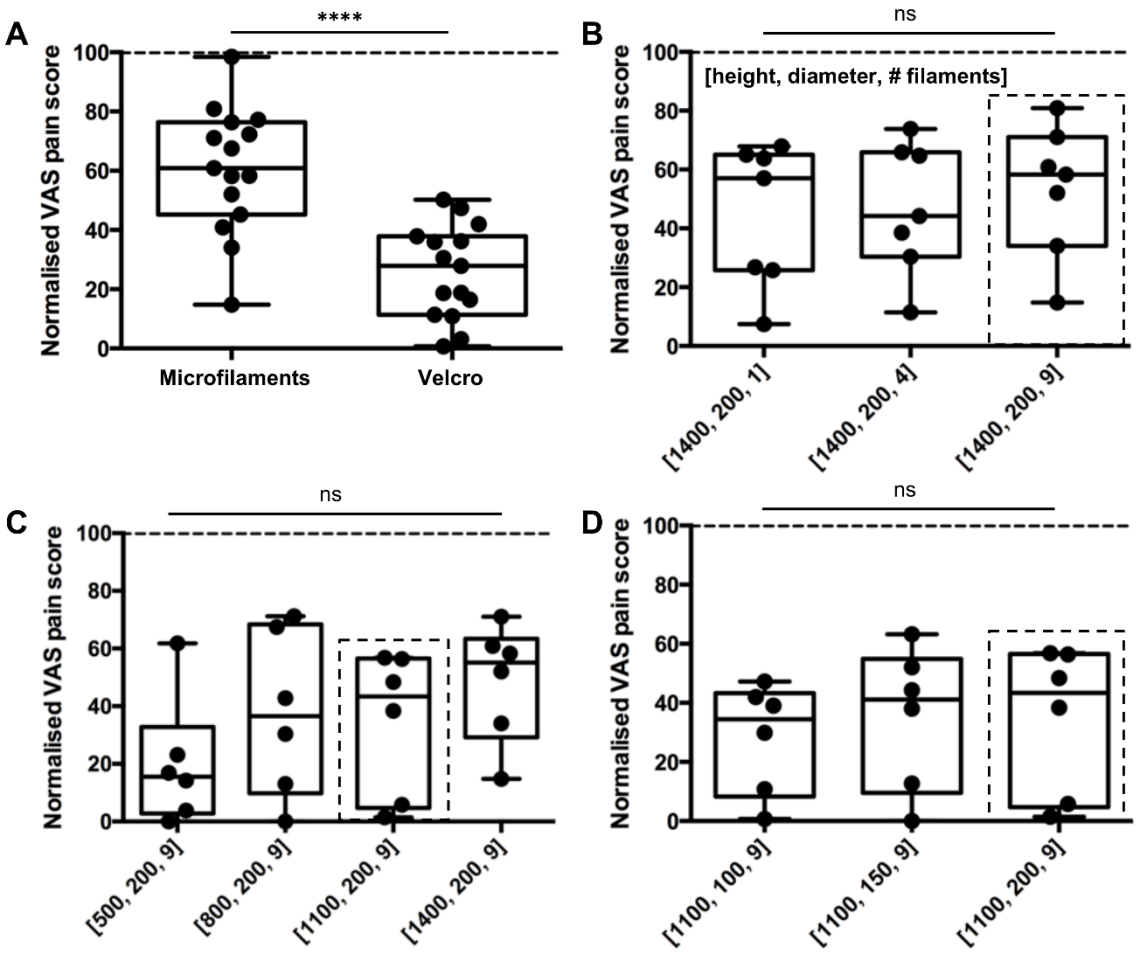

Figure S6. Normalized VAS pain score from human subjects, related to Figure 4A. (A) Box plots of VAS pain scores for 3x3 array of microfilaments or Velcro patch normalized to a 26-gauge hypodermic needle (n=15). (B) Box plots of VAS pain scores normalized to a 26-gauge hypodermic needle for microfilament arrays with variable number of microfilaments (n=7). (C) Box plots of VAS pain scores normalized to a 26-gauge hypodermic needle for 3x3 array with microfilaments of variable height (n=6). (D) Box plots of VAS pain scores normalized to a 26-gauge hypodermic needle for 3x3 array with microfilaments of variable diameter (n=6). The dotted lines indicate the design that was identified as optimal for each group. Data analyzed using a one-way ANOVA with Sidak post-hoc test. “ns” indicates not significant, and “****” indicates significant at $p < 0.0001$. Line indicates comparison between groups.

Supplemental Tables

				AAm/MBAm Ratio		
				15	17.5	20
%AAm (%w/v)	20	λ	470 nm	0.062 ± 0.003	0.055 ± 0.002	0.052 ± 0.002
			520 nm	0.057 ± 0.002	0.051 ± 0.001	0.048 ± 0.002
			550 nm	0.055 ± 0.003	0.049 ± 0.001	0.047 ± 0.002
			580 nm	0.054 ± 0.003	0.048 ± 0.001	0.045 ± 0.002
	25	λ	470 nm	0.065 ± 0.004	0.059 ± 0.006	0.051 ± 0.001
			520 nm	0.063 ± 0.005	0.056 ± 0.007	0.047 ± 0.001
			550 nm	0.062 ± 0.005	0.055 ± 0.008	0.046 ± 0.001
			580 nm	0.061 ± 0.006	0.054 ± 0.008	0.045 ± 0.001
	30	λ	470 nm	0.058 ± 0.009	0.057 ± 0.006	0.054 ± 0.005
			520 nm	0.054 ± 0.009	0.055 ± 0.006	0.050 ± 0.003
			550 nm	0.054 ± 0.009	0.054 ± 0.006	0.048 ± 0.003
			580 nm	0.054 ± 0.009	0.054 ± 0.006	0.048 ± 0.003

Table S1. Absorbance of polyacrylamide at 470 nm, 520 nm, 550 nm, and 580 nm, related to Figure 2B. Absorbance for polyacrylamide formulations with variable acrylamide percentage (%AAm) and ratio of acrylamide to N'N-methylenebisacrylamide crosslinker (AAm/MBAm). Data are represented as mean ± standard deviation.

Transparent Methods

Procedure for Measuring Hydrogel Absorbance

Polyacrylamide precursor solutions consisting of acrylamide (AAm) (Polysciences; Warrington, PA), 2% w/v cross-linking agent N'N-methylenebisacrylamide (MBAm) (Sigma-Aldrich, Allentown, PA), and photoinitiator 2-hydroxy-2-methylpropiophenone (Darocur 1173; BASF Corporation; Florham Park, NJ) were prepared in deionized water. Polyacrylamide disks (diameter: ~6.4 mm, thickness: ~6 mm) of different compositions (%AAm of [20, 22.5, 25, 27.5, 30] and AAm/MBAm ratios of [10, 12.5, 15, 17.5, 20]) were cast in a 96-well flat bottom plate and photopolymerized under a collimated UV light source (365 nm, power ~1.8 mW/cm^2) (Omnicure series 2000; Lumen Dynamics Group; Mississauga, ON) for 10 seconds. The absorbance was then read at the peak excitation and emission wavelengths for FAM, 470 nm and 520 nm, and TAMRA, 550 nm and 580 nm, using a plate reader (Synergy H1; BioTek; Winooski, VT). The reported absorbance values of the hydrogels were computed by subtraction of the average absorbance due to the well plate surface. Percentage of transmittance values can also be inferred from the absorbance values by the following equation:

$$\text{Absorbance} = 2 - \log_{10} \% \text{ Transmittance}$$

A two-way ANOVA was used to assess the significance of the %AAm and AAm/MBAm ratio. Multiple t-tests with the Tukey correction was used to compare groups.

Procedure for Determining Young's Modulus and Shrinkage Percentage

Polyacrylamide disks of different compositions (%AAm of [20, 25, 30] and AAm/MBAm ratios of [15, 17.5, 20]), cast in a 96-well plate, were desiccated and stored at room temperature for at least 2 days following polymerization to allow for complete drying prior to testing. Before performing mechanical testing, the dimensions of each disk were measured using a Vernier caliper. These measurements were used to calculate the shrinkage percentage. To measure the stiffness of desiccated polyacrylamide, compression test was performed using a materials testing machine (Instron 8841 Microtester; Instron; Norwood, MA), equipped with stainless steel platens and a 250-lb load cell. Using integrated Instron software, the platens were brought into contact with the disk sample on the stage until a 10 gf (0.098 N) preload was reached. Then compression over a displacement of 500 µm was applied at a rate of 0.001 mm/s. The integrated software was used to track the displacement of the platens and the readings of the load cell. This procedure was repeated to determine the Young's modulus for PEEK disks using a 450-lb load cell.

To determine the Young's modulus of the hydrated hydrogel, a custom unconfined compression device was used equipped with a 250-gf load cell. After reaching a preload of 2 gf, the hydrogel was compressed to 90% of the unloaded thickness at a strain rate of 0.05%.

For all samples, the Young's modulus was calculated by dividing the difference between the preload and equilibrium load by the sample area times the percent strain.

$$\text{Young's Modulus} = \frac{\text{Equilibrium load} - \text{Preload}}{\text{Area}} \cdot \frac{1}{\% \text{ Strain}}$$

A two-way ANOVA was used to assess the significance of the %AAm and AAm/MBAm ratio with a Tukey post-hoc test applied for multiple comparisons.

Procedure for Determining Diffusion Coefficient for 2-NBDG

Glass slides were treated with 0.48% v/v 3-(trimethoxysilyl)propyl methacrylate (TMSM) (Sigma-Aldrich; Allentown, PA) and 2.90% glacial acetic acid in ethanol for 3 minutes and then rinsed with ethanol. Polyacrylamide hydrogel with 30% AAm and AAm/MBAm ratio of 15 was polymerized to form 5 x 5 x 0.5 mm slabs on the glass slide. The hydrogel was incubated overnight in a 8 x 8 x 5 mm well containing a solution of fluorescent glucose analog 2-(N-(7-nitrobenz-2-oxa-1,3,-diazol-4-yl)amino)-2-deoxyglucose) (2-NBDG) (Thermo Fisher Scientific; Eugene, OR). Fluorescence recovery after photobleaching (FRAP) was then performed by using a confocal microscope (Leica TCS SP5 Confocal and Multi-Photon Microscope; Wetzlar, Germany). Firstly, a circular region of diameter 20 µm was bleached through the

fluorescent hydrogel using 488 nm Argon laser set at 95% power. The hydrogel was subsequently images at a lower power of 6% as to avoid further bleaching. Fluorescence recovery in the bleached region was imaged every 0.229 seconds for 45 seconds, allowing for determination of the lateral transport rate, in the idealized case of pure two-dimensional diffusion monitored by a uniform circular disc profile. The diffusion coefficient is determined from an experimental recovery curve $\hat{f}$, using the following equation:

$$D = \left(\frac{w^2}{4\tau_{1/2}}\right)\gamma_D$$

where w is the radius of the disc, γ_D is 0.88, and $\tau_{1/2}$is the time for which $\hat{f}(\tau_{1/2}) = \frac{1}{2}$.

Four separate FRAP experiments were performed for four independently prepared samples. The mean diffusion coefficient from the repeated FRAP experiments was taken to represent the sample, and the mean and standard deviation of the independently prepared samples were computed.

Fabrication of PEEK Microfilament Arrays for Human Subject Assessment

Microfilament arrays were designed using SolidWorks CAD Software (SolidWorks, Concord, MA) and fabricated via CNC milling of polyether ether ketone (PEEK) (McMaster-Carr; Robbinsville, NJ), a medical-grade biocompatible plastic with high mechanical strength, using Haas MiniMill 4x (Haas Automation; Oxnard, CA). Each array has a diameter of 7 mm and contains 1, 4, or 9 microfilaments in a 1x1, 2x2, or 3x3 configuration; the microfilaments are 500, 800, 1100, or 1400 µm tall, 100, 150, or 200 µm in diameter, have a 74° diamond-shaped bevel, and are spaced 1500 µm apart tip-to-tip. To sterilize, each microfilament array was disinfected by sonication in two fresh baths of 70% ethanol, air-dried, and steam sterilized at 121°C for 30 minutes. After sterilization, the PEEK microfilament devices were left in the sealed pouch in a sterile environment until use.

Pain Assessment and Healing Response in Human Subjects

All pain assessments on human subjects were approved by the Institutional Review Boards at Columbia University Medical Center, and research was carried out with informed consent from the subjects. Human subjects were recruited form the students and staff population at Columbia University. Susceptibility to hypodermic scarring was used as the subject exclusion criterion. Overall, 6 males and 9 females (ages 19-56) participated in this study. The level of pain experienced due to the application or insertion of the device in question was measured using the visual analogue scale (VAS), as previously described (Hawker et al., 2011). Controls for this experiment include: 26-guage hypodermic needle as the positive control, a flat circular surface of PEEK rod of 7 mm diameter as the negative control; and the hook surface of a hook-and-loop fastener as a comparison. Application or insertion of the device was performed manually on randomized locations of the subject's volar forearms, previously cleaned with isopropanol swabs by the investigator. All experiments began with the insertion of the PEEK microfilament array, the negative, and the positive controls to help the subjects calibrate their response to the range of sensations to be encountered on the VAS scale. Each treatment lasted ~10 seconds, and the pain level indicated on the VAS scale by the subject for each treatment was recorded. All insertions were performed in triplicate for every subject, and in random sequence. For each subject, average raw VAS pain score for each of the devices assessed were calculated and normalized to the average raw hypodermic 26-guage needle pain score to account for the variability in a subject's perception and to provide a common reference point.

6 of the 15 subjects were used to determine the effects of microfilament length, diameter, and the number of microfilaments in an array on insertion pain. The study was carried out in two stages, in order to avoid carryover effects from too many insertions. In the first stage, the effects of microfilament length and number of microfilaments in an array were investigated. The PEEK microfilament devices tested in this stage included (denoted [length (µm), diameter (µm), number of microfilaments]) [500, 200, 9]; [800, 200, 9]; [1400, 200, 9]; [1400, 200, 4]; and [1400, 200, 1]. In the second stage, the effects of diameter

were investigated using the devices of [1100, 100, 9]; [1100, 150, 9]; and [1100, 200, 9]. The two stages were separated by a minimum of 20 minutes of break.

To assess the healing response after insertion and removal of PEEK microfilament arrays, images of the skin surface were capture at multiple points after device removal.

A one-way ANOVA was used to assess the significance of the designs and geometries with a Sidak post-hoc test applied for multiple comparisons.

Fabrication of Polyacrylamide Microfilaments Arrays

Positive microfilament array molds were designed using SolidWorks CAD Software (SolidWorks; Concord, MA) and fabricated via CNC milling machinable acrylic plastic (McMaster-Carr; Robbinsville, NJ) using Haas MiniMill 4x. Silicone negative mold is then replicated from the positive mold with Dragon Skin platinum silicone (10 Medium; Smooth-On; Macungie, PA) with the two components mixed in the ratio of 1:1, degassed and cured on the acrylic molds at 60°C for 4 hours. The cured silicone mold is removed from the acrylic master, rinsed in water and 70% ethanol, and wet autoclaved. Microfilament arrays were prepared by casting polyacrylamide precursor solution in the negative silicone mold and photopolymerized under a collimated UV light source.

Measurement of Microfilament Penetration and Failure Forces

Full-thickness human cadaver skin was obtained from the Columbia University Anatomical Gift Program with approval from the Columbia University Medical Center Institutional Review Boards, and used according to the Declaration of Helsinki Principles. The skin was derived from the abdominal region. Full ethical and regulatory approval was obtained from Columbia University Medical Centre Institutional Review Boards for use of all these tissues and the subsequent experimentation. The skin samples were stored at -20°C until use. Before use, the skin tissue was allowed to thaw at room temperature for 2 hours, and cut into ~2 x 2 cm pieces followed by immersion in PBS for 2 hours. A flat section of skin tissue was affixed using cyanoacrylate glue to a test fixture and mounted on the base platen of the Instron 8841 Microtester. The microfilament array (3x3 array and 7 mm diameter) or a flat polymer disk was glued onto the opposing test fixture and fixed on the upper platen of the mechanical tester. Test samples were brought into contact with the tissue until a 10 gf (0.098 N) preload was reached. The samples were then displaced at a rate of 0.02 mm/s, and the force was recorded for insertion. The samples were displaced at the same rate of 0.02 mm/s in the opposite, and the force was recorded for removal.

Mechanical failure of microfilaments was considered due to axial loading and traverse loading. To measure the force a microfilament can withstand before failure under an axial load (i.e. force applied parallel to the microfilament axis), the microfilament array on the upper platen was pressed against the rigid metal surface of the base platen at 1 mm/s. Upon failure, the force suddenly dropped; the maximum force applied immediately before dropping was interpreted as the force of needle failure. Microfilaments were examined by microscopy (SZX2-ILLK, Olympus) before and after failure testing to determine the mode of failure, e.g. buckling failure due to inelastic or elastic instability. Data were discarded if only some of the microfilaments were broken. Data are reported as the force per microfilament for failure.

Interstitial Fluid Sampling in Hairless Rats

Polyacrylamide microfilament arrays were fabricated using a polymer composition of 30% w/v AAm, 2% w/v MBAm, 0.5% v/v Darocur 1173. The microfilament arrays were placed on a CD hairless rat (Charles River; Raleigh, NC) and allowed to equilibrate. The rat was anaesthetized by isoflurane inhalation (Isothesia; Henry Schein Animal Health; Dublin, OH) delivered at 1.5 mL/h via an E-Z Anesthesia (E-Z Systems Corp; Palmer, PA), and its body temperature was maintained at 37°C using a warm water recirculating heat pad. The microfilament arrays were inserted into the skin by a gentle press and secured in position with skin adhesive (Tegaderm; 3M; Appleton, WI). After being worn on rat skin for 1 hour, the microfilament arrays were removed and subsequently treated with silver nitrate solution (Sigma-Aldrich; Allentown, PA) to detect the presence of chloride ions from the interstitial fluid. For visualization purposes, the red and yellow channels were boosted to highlight the silver deposits. All animal studies were approved by the Columbia University Institutional Animal Care and Use Committee.

Histological Preparation
Polyacrylamide microfilament arrays were fabricated using a polymer composition of 30% w/v AAm, 2% w/v MBAm, 0.5% v/v Darocur 1173. The microfilament arrays were placed on a CD hairless rat. All microfilament arrays were worn on rats for at least 24 hours before removal. After the rats have been sacrificed, the insertion sites were excised from the bulk skin with a scalpel. Samples were obtained immediately, 30 mins, 1 hour, 2 hours and 4 hours after removal of microfilament array from hairless rat skin. The isolated skin pieces were placed in cryostat molds embedded with optimum cutting temperature (OCT) media (Tissue-Tek, Torrance, CA). The skin was fixed in OCT by freezing the sample on dry ice. Frozen skin samples were sliced into 12-µm thick sections (Cryo-star HM 560MV, Microm, Waldorf, Germany). The skin sections were stained with hematoxylin and eosin using an automated staining machine (Leica Autostainer XL, Nussloch, Germany). After staining, the sections were covered with glass slides sealed with cytoseal 60 (low viscosity, Richard-Allan Scientific, Kalamazoo, MI). The sections were dried overnight before taking images under the microscope (Leica TCS SP5 Confocal, Wetzlar, Germany). All animal studies were approved by the Columbia University Institutional Animal Care and Use Committee.

Aqueous Emission Spectra and Peak Emission Curve
Oligonucleotide aptamer with L-phenylalanine binding site, 6-carboxyfluorescein (FAM) and 6-carboxytetramethylrhodamine (TAMRA) fluorophore reporting unit, and 5'-acrydite modification (Integrated DNA Technologies; Coralville, IA) was prepared to 200 nm using phosphate buffered saline with 2 mM $MgCl_2$ (PBS). The aptamer solution was placed in boiling water for 5 minutes then allowed to cool for 30 minutes. Aliquots of the prepared aptamer sensor were added to equal volume aliquots of phenylalanine (Sigma-Aldrich, Allentown, PA) solutions prepared via serial dilution from 1000 µM to 1.95 µM. The aptamer-phenylalanine solutions were allowed to react for 40 minutes before being pipetted into a black 96-well clear, flat bottom plate. The fluorescence was read in a plate reader with λ_{ex} = 470 nm and λ_{em} scanned between 500 and 650 nm. The fluorescence intensity at 520 nm was used to construct the curve showing concentration dependence at peak fluorescence emission.

Aqueous Response Time
200 nM aptamer sensor solution was prepared in PBS. The aptamer solution was placed in boiling water for 5 minutes then allowed to cool for 30 minutes. Aliquots of aptamer solution were combined with equal volume aliquots of PBS and pipetted into a 96-well plate. The fluorescence was read in a plate reader with λ_{ex} = 470 nm and λ_{em} = 520 nm. These readings served as the values for t = 0 seconds. Next, aliquots of the 200 nM aptamer solution were pipetted into the 96-well plate. Equal volume aliquots of 500 µM phenylalanine solution was then added into the same wells. The plate was quickly placed in the plate reader, and the fluorescence was read with λ_{ex} = 470 nm and λ_{em} = 520 nm with a read taken every 7.5 sec. A stopwatch was used to determine the time between addition of the phenylalanine aliquot and the first fluorescence reading.

Aqueous Photobleaching
200 nM aptamer sensor solution was prepared in PBS. The aptamer solution was placed in boiling water for 5 minutes then allowed to cool for 30 minutes. Aliquots of aptamer solution were combined with equal volume aliquots of PBS with 1000 µM phenylalanine and allowed to react for 40 minutes. The solution was then pipetted into a 96-well plate. The fluorescence was read in a plate reader with λ_{ex} = 470 nm and λ_{em} = 520 nm. Fluorescence readings were taken repeatedly to assess the effects of photobleaching.

Hydrogel Emission Spectra and Peak Emission Curve
A polyacrylamide precursor solution of 30% w/v AAm, 2% w/v MBAm, and 100 nM aptamer sensor was prepared in PBS. The precursor solution was placed in boiling water for 5 minutes then allowed to cool for 30 minutes. Next, 0.5% v/v of Darocur 1173 was added. The monomer solution was polymerized into disks ~5.6 mm diameter and ~2.3 mm height. The disks were then placed in PBS with the specified phenylalanine concentration prepared via serial dilution from 500 µM to 0.98 µM and soaked overnight. The disks were then removed from the phenylalanine solution, dried with a Kimwipe, and placed in a 96-well plate. The fluorescence was read in a plate reader with λ_{ex} = 470 nm and λ_{em} scanned between 500 and 650 nm. The fluorescence intensity at 520 nm was used to construct the curve showing concentration dependence at peak fluorescence emission.

Hydrogel Response Time
A polyacrylamide precursor solution of 30% w/v AAm, 2% w/v MBAm, and 100 nM aptamer sensor was prepared in PBS. The precursor solution was placed in boiling water for 5 minutes then allowed to cool for 30 minutes. Next, 0.5% v/v of Darocur 1173 was added. The monomer solution was polymerized into disks of ~6.4 mm diameter and ~1 mm height in a 96-well flat bottom plate. PBS was added to a subset of disks, and the fluorescence was read in a plate reader with λ_{ex} = 470 nm and λ_{em} = 520 nm. These readings served as the values for t = 0 seconds. Next, 500 µM phenylalanine solutions were added to the wells with the remaining disks. The fluorescence was read with λ_{ex} = 470 nm and λ_{em} = 520 nm with a read taken every 70 seconds.

Hydrogel Leaching
A polyacrylamide precursor solution of 30% w/v AAm, 2% w/v MBAm, and 100 nM aptamer sensor was prepared in PBS. The precursor solution was placed in boiling water for 5 minutes then allowed to cool for 30 minutes. Next, 0.5% v/v of Darocur 1173 was added. The monomer solution was polymerized into disks of ~5.6 mm diameter and ~2.3 mm height. A subset of disks was placed in a small volume of PBS (~50 µL per disk) and allowed to soak for 2 hours to ensure they were fully hydrated. Next, the disks were removed from the PBS, dried with a Kimwipe, and placed in a 96-well plate. The fluorescence was read in a plate reader with λ_{ex} = 470 nm and λ_{em} = 520 nm. The remaining disks were placed in an excess of PBS and soaked overnight. The next day, a subset of disks were again removed and the fluorescence was read. The remaining disks were then placed in a fresh excess of PBS. This procedure was repeated 3 more times with the disks read and the PBS changed daily. This experiment was repeated as specified, but the aptamer sensor was substituted with a sensor without the 5'-acrydite modification to serve as a control. A two-tailed t-test was used to compare the endpoint fluorescence between the two groups.

Hydrogel Reversibility
A polyacrylamide precursor solution of 30% w/v AAm, 2% w/v MBAm, and 100 nM aptamer sensor was prepared in PBS. The precursor solution was placed in boiling water for 5 minutes then allowed to cool for 30 minutes. Next, 0.5% v/v of Darocur 1173 was added. The monomer solution was polymerized into disks of ~5.6 mm diameter and ~2.3 mm height. The disks were then placed in PBS and allowed to soak for 2 hours to ensure they were fully hydrated. Next, a subset of disks was removed from the PBS, dried with a Kimwipe, and placed in a 96-well plate. The fluorescence was read in a plate reader with λ_{ex} = 470 nm and λ_{em} = 520 nm. The remaining disks were then transferred to PBS with 250 µM of phenylalanine and allowed to soak for 1 hour. The disks were then removed and placed in a fresh solution of PBS with 250 µM of phenylalanine and soaked for an additional hour. A subset of disks was then removed, dried with a Kimwipe, and placed in a 96-well plate. The fluorescence was read in a plate reader with λ_{ex} = 470 nm and λ_{em} = 520 nm. This procedure was repeated for the remaining reads at different phenylalanine concentrations in the order of 500 µM, 250 µM, 0 µM, 250 µM, 500 µM.

Statistical Analysis
Statistical tests were calculated in GraphPad Prism 8.1. The details of the statistical tests are indicated in the respective figure legends. Where data was assumed to be normally distributed, values were compared using a one-way ANOVA for single variable with a Sidak post-hoc test applied for multiple comparisons. Where data was assumed to be normally distributed, values were compared using a two-way ANOVA for more than one variable with a Tukey post-hoc test applied for multiple comparisons.